AN ABSTRACT OF THE THESIS OF

[Master of Science]

Koji Kobune (Name) for the degree of Civil Engineer (Degree)

in Civil Engineering (Major Department) presented on December 13, 1977

Title: Random Wave Velocity Field From Periodic Theory

Redacted for Privacy

Abstract approved: Dr. John H. Nath

Random waves are often expressed as a mathematical superposition of an infinite number of sinusoidal components. The mean square spectral density of the water surface elevation is often called the wave spectrum. The zero upcrossing wave heights usually have a Rayleigh probability distribution. However, the design wave concept is still used for design of many marine structures. It is common to use periodic wave theory to predict the velocity distribution in the design wave even though it is known that actual waves are quite irregular and their shape and kinematics may not conform to the periodic theory.

The purpose of this study is to examine the validity of applying periodic wave theory to a wave in a random wave train. The magnitude of the errors are quantified in a statistical manner. The experiments were conducted in the Wave Research Facility at Oregon State University wherein random waves were generated with a flap-type wave board, resulting in a Bretschneider type spectrum with significant wave heights from 2.0 to 2.8 feet and significant periods from 2.5 to 2.8 seconds.

The water particle velocities were measured with a hot film anemometer.

The observed maximum horizontal and vertical velocities of each zero upcrossing wave were compared with predicted ones from the linear wave theory. The relative error is expressed as

$$\varepsilon = \frac{u_{measured} - u_{predicted}}{u_{predicted}} \quad .$$

The relative error turned out to be normally distributed and the standard deviation varied from 0.1 to 0.6 according to the size of the wave sample, although the mean value of the error remained almost constant. The error was smallest for the large waves which gives confidence to use of periodic theories for the design wave concept even though random waves are experienced by the structure.

Random Wave Velocity Field From Periodic Theory

by

Koji Kobune

A Thesis

Submitted To

Oregon State University

in partial fulfillment of
the requirements for the
degree of

Civil Engineer

Completed December 13, 1977

Commencement June 1978

APPROVED :

Redacted for Privacy

Professor of Mechanical Engineering
in charge of major

Redacted for Privacy

Head of Department of Civil Engineering

Redacted for Privacy

Dean of Graduate School

Date thesis is presented December 13, 1977

Typed by the researcher for Koji Kobune

ACKNOWLEDGEMENT

The study presented herein was conducted in the Ocean Engineering Programs at Oregon State University under the supervision of Dr. John H. Nath, Professor of Mechanical Engineering and the Director of Environmental Fluid Dynamics Laboratory. The author sincerely wishes to express his appreciation to Dr. John H. Nath for his helpful advice from the planning of the experiments to the analyses of the results and for his critical review of the manuscript.

The author also wishes to express his hertfelt thanks to Dr. Tokuo Yamamoto, Dr. Robert T. Hudspeth and Dr. Charles K. Sollitt, Professors of Civil Engineering, for their suggestions in the data analyses, and to Mr. Terry Dibble and Mr. Larry Crawford, Technical Staff Members of the Ocean Engineering Program, for their kind assistance in the experiments.

The wave kinematics from Stokes' fifth order theory and the spectra of the test random waves were computed by the Digital Computer CYBER 71 Series at Oregon State University Computer Center. The author owes his thanks Mr. Robert Jensen, ex-graduate student in the Ocean Engineering Program, for his generous permission to use his computer program, Stokes' fifth order theory.

TABLE OF CONTENTS

LIST OF ILLUSTRATIONS

List of Tables

List of Photos

List of figures

RANDOM WAVE VELOCITY FIELD FROM PERIODIC THEORY

1 INTRODUCTION

Two different methods have been developed to represent random ocean waves for the prediction of wave forces on marine facilities. One is a conventional method which uses the design wave concept designated by a height (H_D) and period (T_D) and direction. The other utilizes the mean square spectral density of the water surface fluctuation which is often called the wave spectrum.

The latter method has become of interest for the dynamic analysis within the design of marine structures, such as offshore oil facilities. These structures are less stiff in comparison with massive structures such as sea walls and breakwaters, and their stability should be examined against the continuous random wave action. Thus, many studies on random wave - structure dynamic interaction have been made, and the validity of this analysis is being confirmed.

On the other hand. the design of many other marine facilities are still dependent on the first method. These structures are stiff and can be designed to resist waves by means of static analysis.

In the process of the design wave method, a design wave is chosen to represent a severe sea condition for the structure in a depth of water, h. The design wave is characterized by its height, H_D, and its period, T_D, which are determined on the basis of a statistical study, wave records, hindcasting, experience and judgement. The design wave height is usually a large, rare value, and sometimes can be specified

as some factor (e.g. 2.0) times the significant wave height (the average of the one-third highest waves).

The water kinematics within a thus chosen design wave are estimated by fitting a periodic wave to the design wave and utilizing an appropriate periodic wave theory. However, the design wave as it occurs in nature may have an irregular profile rather than a smooth profile as given by the wave theory.

The purpose of this study is to examine the validity of the design wave method by estimating the magnitude of error to be expected when periodic wave theories are used to predict the water kinematics within random waves.

Random waves were generated in the Wave Research Facility at Oregon State University. Discrete zero upcrossing waves were selected to compare the measured ones. The results show that the periodic wave theory do adequately predict water particle velocities for the large waves. This is fortunate because the design wave method is used with the large waves.

2 LITERATURE SURVEY

2.1 Velocity measurements in random waves

Studies of random waves concerning wave forces have been conducted from increasing requests for the construction of submarine pipe lines and large pile supported marine structures. In these studies, the dynamic structure responses, such as bending moment imposed on the structure members and deflection of a whole structure, are of principal interest. Thus, many efforts have been made to develop mathematical models of wave-structure interaction on the basis of linear superposition of sinusoidal waves: R.O. Reid (1), L.E. Borgman (2), J.H. Nath and D.R.F. Harleman (3). The availability of these mathematical models to predict the kinematics of random waves can not be confirmed until they are examined through velocity and acceleration measurements.

Y. Iwagaki et. al. (4) measured water particle velocities of random waves utilizing a sonic doppler current meter. They found that Reid's numerical filter (5) given by Equation (2.1) and (2.2) provided a fairly good estimate of the time variation of wave kinematics, given the time series of the water surface elevation $n(t)$.

$$u(t) = a_0\, n(t) + \sum_{m=1}^{N} a_m \left[n(t+m\tau) + n(t-m\tau) \right] \tag{2.1}$$

$$w(t) = \sum_{m=1}^{N} b_m \left[n(t+m\tau) - n(t-m\tau) \right] \quad , \tag{2.2}$$

where a_m and b_m are Fourier coefficients in the Fourier expansion of the frequency response functions. That is,

$$a_m = \frac{1}{\pi}\int_0^{\omega_c\tau} R_u(\omega)\ \cos\ m(\omega\tau)\ d(\omega\tau), \quad m = 0,1,2,\ldots,N \tag{2.3}$$

$$b_m = \frac{1}{\pi}\int_0^{\omega_c\tau} R_w(\omega)\ \sin\ m(\omega\tau)\ d(\omega\tau), \quad m = 1,2,3,\ldots,N \tag{2.4}$$

where ω_c is the cut-off frequency, and

$$R_u(\omega) = \frac{\omega\ \cosh\ k(h+z)}{\sinh\ kh} \tag{2.5}$$

$$R_w(\omega) = \frac{\omega\ \sinh\ k(h+z)}{\sinh\ kh}\ . \tag{2.6}$$

and k is the wave number, $2\pi / L$, with L the wave length.

Figure 2.1 shows the comparison of the velocity variation with the water surface elevation of their experiment. It is seen that the horizontal velocity variation closely followed the water surface elevation and its maxima and minima appear at the wave crests and troughs respectively. In addition, the vertical velocity is related to the slope of water surface and the peaks appear when the water surface crosses the still water level. Thus, discrete waves in a random wave train have similar general characteristics to periodic waves.

In addition to the time variation of velocities, the frequency response function was discussed (4). The measured response function, which was defined as Eq. (2.7) and (2.8), turned out to be larger than the response function given by Airy theory, Eqs. (2.5) and (2.6), for the higher frequency range.

$$[\ R_u(\omega)\ ]_{\text{measured}} = \sqrt{\frac{S_{uu}(\omega)}{S_{\eta\eta}(\omega)}} \tag{2.7}$$

$$[\, R_w(\omega) \,]_{\text{measured}} = \sqrt{\frac{S_{ww}(\omega)}{S_{nn}(\omega)}} \qquad (2.8)$$

where $S_{nn}(\omega)$, $S_{uu}(\omega)$ and $S_{ww}(\omega)$ are the power spectral density of water surface elevation, horizontal velocity and vertical velocity, respectively.

They commented that such a difference was partly caused by the noise of the current meter.

Y. Tsuchiya and Yamaguchi (6) measured the velocity of wind generated waves in a recirculation wave tank utilizing the sonic doppler current meter. The results of their measurements yielded similar conclusions to Iwagaki's study because of contamination of the records with noise from the current meter.

Apart from the spectrum analysis, the discussion about the water particle velocities of discrete waves in a random wave train is seen in the study by R.A. Grace and R.Y. Rochelean (7). They measured the near bottom velocities beneath the wave crests and troughs of long period waves (from 14 to 20 seconds) at the Waikiki shore, Hawaii,utilizing a propeller current meter. For this wave period range and water depth, 38 feet(10.6 m), Airy theory gives almost a constant ratio of the horizontal velocity beneath a wave crest, u_+, to the wave height, H. That is

$$u_+ / H = 0.476 \; . \qquad (2.9)$$

The wave height, H_p, was calculated with Airy wave theory from the pressure measured at the bottom. The field work showed that the velocity, u_+, was linearly related to the

wave height H_p just like the relation given by Airy thoery, Eq. (2.9), and that the least-square method yielded the following linear regression relation.

$$u_+ / H_p = 0.544 \tag{2.10}$$

where the wave height, H_p, was defined as the average of the trough to crest height fore and aft the crest. Thus, their definition is different from the zero upcrossing wave height.

The residuals which exist between the measured velocity and the velocity calculated from Eq.(2.10) were examined. The distribution of the residuals turned out to be normal with the mean of -0.006 ft/sec and the standard deviation of 0.238 ft/sec.

As mentioned above, the wave heights used in their comparison were calculated from the measured pressure. These calculated wave heights are usually smaller than true (surface) wave heights(8). This may have caused the difference between the coefficients in Eq. (2.9) and Eq. (2.10). The authors introduced a correction factor, n_c, so that tha true wave heights were estimated by Eq. (2.11)

$$H = n_c H_p \tag{2.11}$$

From Eqs.(2.9) and (2.10), the correction factor is calculated as

$$n_c = 1.15 \tag{2.12}$$

This value is consistent with the value listed by Grace (8).

From the above discussion, the authers concluded that Airy theory provided an excellent prediction of the mean realization of the velocity beneath the wave crests. This can be expressed by the following equation.

$$\frac{1}{N}\sum_{i=1}^{N}[u_+]\text{ predicted by Airy theory}$$

$$= \frac{1}{N}\sum_{i=1}^{N}[u_+]_{\text{measured}} \tag{2.13}$$

2.2 Velocity measurement equipment

Accurate measurements of the water particle velocities in wave motion are difficult to make, and a variety of equipment has been used.

2.2.1 Propeller current meter

Propeller current meters are common instruments to measure quasi-steady flows such as wind, open channel flow, flow in ducts, tidal flow and so on. However there is a difficulty in using them in waves, especially in laboratory wave tanks, because of usual low dynamic response to high frequency fluctuations. In addition, they are usually not very sensitive to low speed steady flow.

Y. Goda (9) overcame the difficulty by utilizing small propellers (diameters of 3.5 cm) and a large wave tank (water depth: from 1 m to 2 m, wave height: from 15 cm to 80 cm and wave period: from 2 sec to 8 sec). Based on the experiments, he proposed the following empirical formula to estimate the horizontal velocity beneath the wave crests.

$$u_+ = \sqrt{1 + \alpha\left(\frac{H}{h}\right)^{\frac{1}{2}}\left(\frac{s}{h}\right)^3}\cdot\pi\frac{H}{T}\frac{\cosh ks}{\sinh kh} \tag{2.14}$$

where α is a coefficient which varies from 1.5 to 0.25 depending on the ratio of the water depth to the wave length h/L_A, H is the wave height, T is the wave period, L_A is the wave length given by Airy theory, $k=2\pi/L_A$ and s is the distance from the bottom. Goda gave the coefficients, α, for

various conditions as shown in Table 2.1.

Equation (2.14) modifies the horizontal velocity given by Airy theory in order to correctly express the large velocity near the still water level. According to the comparison among the available theories done by Dean (10), Eq. (2.14) gives as good a fit with measured velocities as Dean's Stream Function Theory. Hence, Dean's Stream Function Theory gives good estimates of the horizontal velocity beneath the wave crests.

2.2.2 Photographic method

The water particle motion can be visualized with tracers, such as neutrally buoyant particles and/or hydrogen bubbles. Thus, the particle velocities in waves can be measured with the aid of a high speed movie camera. This method is suitable for experiments in small wave tanks. Measurements from this method have provided much information of the kinematics of finite amplitude waves: LeMehaute(11), Dean(12) and Iwagaki (13).

2.2.3 Hot film anemometer

Hot film and hot wire anemometers are commom instruments for the measurement of turbulence in air flows. They have been improved so that they can be operated in water as well as in the air. Their characteristics in water have been examined by many researchers, some of whom are Richardson and McQuivey(14), Morrow and Kline(15) and Kato and Sano(16).

However, besides the usual difficulties in the operation of hot film anemometers, such as zero velocity drift due to the fluid temperature change and the accumulation of dirty materials on the sensor, there are some inconveniences when they are used for velocity measurements in waves. A hot film sensor is sensitive to the magnitude of a flow speed and it can not

detect the flow direction when the velocity vector is in the plane perpendicular to the hot film axis. Another is the strong non-linearity in the correlation between the flow speed and the output voltage when the flow speed varies over a wide range. In addition, the film is sensitive to to flows that are parallel to the film axis.

Y. Iwagaki and T. Sakai(13) used a pair of hot film anemometers to measure the water particle velocity near the bottom, where the vertical velocity component vanishes and the output voltage corresponds to the magnitude of the horizontal velocity. They operated two probes simultaneously: one was used to measure the velocity during the passage of wave crests and the otherwas used during the passage of wave troughs. The records from these two probes were connected at the times when the voltages of these two are equal.

The results show that measured velocity variations were similar to Stokes third order theory(17) for intermediate water condition and Hyperbolic waves(18) for shallow water conditions.

Some methods to measure water particle velocities in the upper region rather than near the bottom region have been developed by Kolpak and Eagleson (19) and Van Dorn and Pazan(20). The former used a small direction vane to detect the flow direction, and compared the results with thoses measured by photographic methods. They found the resulting directional error to be small enough when the ratio of the vane width to the radius of curvature of the water particle orbit was less than 0.1. In addition, they cautioned that high sensor operating temperature might cause contamination of the record due to heated wakes for a stationary probe.

Van Dorn used an orthogonal pair of wedge type hot film probes and

measured the velocity distribution at the crests of near breaking waves. The procedure to obtain the magnitude and the direction of the flow is complicated. The principle can be summerized as follows.

Suppose the orthogonal pair of the hot film probes are installed as shown in Fig. 2.2, and the range of θ is limited within the range from $-\pi/4$ to $\pi/4$. The non-linear output voltages from these probes have the following relation with the magnitude of the flow speed, V, and the direction, θ.

$$(E_B^2 - E_0^2)_1 = V^n \alpha_1(\theta_1) = V^n \alpha_1(\tfrac{\pi}{4} + \theta) \tag{2.15}$$

$$(E_B^2 - E_0^2)_2 = V^n \alpha_2(\theta_2) = V^n \alpha_2(\tfrac{\pi}{4} - \theta) \tag{2.16}$$

where E_B is the non-linear output voltage, E_0 is the zero flow output voltage, n is a coefficient, $\alpha(\theta)$ is a directional coefficient and the suffix 1 and 2 show the variables are concerning probe 1 and probe 2, respectively. The coefficients n and $\alpha(\theta)$ and the zero flow output voltage E_0 are determined through calibrations.

From Eq. (2.15) and (2.16), the following equations are obtained.

$$\frac{(E_B^2 - E_0^2)_1}{(E_B^2 - E_0^2)_2} = \frac{\alpha_1(\frac{\pi}{4} + \theta)}{\alpha_2(\frac{\pi}{4} - \theta)} \tag{2.17}$$

For the measured ratio $(E_B^2 - E_0^2)_1 / (E_B^2 - E_0^2)_2$, the flow direction θ can be found from a table of $\alpha_1(\frac{\pi}{4} + \theta) / \alpha_2(\frac{\pi}{4} - \theta)$.

Having found θ, the corresponding flow speed V is calculated by either equation Eq. (2.15) or Eq. (2.16).

2.2.4 Ultra sonic doppler current meter and laser doppler anemometer

As mentioned in Section 2.1 and shown in Fig. 2.1, ultra sonic doppler current meters have been used to measure the velocities in random waves, and have brought fruitful results. This current meter can be operated not only in laboratory wave tanks but also in the ocean as described in Tsuchiya and Yamaguchi(6).

Recently the laser doppler anemometers have been developed. Lee, Grated and Durrani(21) tested this anemometer in periodic and random waves. They reported that it was a highly suitable instrument for laboratory study of waves. A full discussion about the kinematics of random waves, however, is not given in this paper.

3 FACILITIES AND EQUIPMENT

3.1 Wave tank and wave generator

All the experiments were conducted in the Wave Research Facility at Oregon State University. The wave tank is 342 feet (104 m) long, 12 feet (3.7 m) wide and 15 feet (4.6 m) deep except near the wave board, where the bottom of the tank is three feet deeper than the main part. The wave absorber is a concrete beach with a slope of one on twelve. The reflection coefficient of this beach is reported to be from 2.8 % to 11.8 % for the wave periods ranging from 0.95 seconds to 5.06 seconds (22). Figure 3.1 shows the general view of the wave tank.

The wave generator is in the deeper end of the tank and has a flap type wave board. The wave board is driven by a hydraulic piston which is controlled by a potentiometric hydraulic servo system. The servo system is activated by an electric input, which can be either sinusoidal or random signal.

3.2 Measurement of water surface elevation

The water surface elevations for this work were measured with a Sonic System Model 86 Sonic Wave Profiler. The system operates by measuring the travel time required for a sound pulse to propagate from the sound source (a spark) to the water surface and return to the microphone. A signal conditioner converts the travel time to distance and from this the oscillating water surface is defined.

3.3 Measurements of velocity

The water particle velocities were measured utilizing two kinds of instruments: 1) a Nover Nixon Streamflo probe 403 propeller current meter, and 2) a Thermo System Inc. (TSI) 1240-60w X-type cylindrical hot film probe coupled with TSI Model 1050 constant temperature anemometers and Model 1052 Linearizers. These two probes were installed on the side walls of the wave tank (see Fig. 3.2).

3.3.1 Nover Nixon Streamflo propeller probe (Photo 3.1)

The propeller of the probe has a diameter of 0.47 inches(1.2 cm) as shown in Fig. 3.3. It is composed of five blades mounted on a hard stainless steel spindle. Both ends of the spindle are fine burnished conical pivots which run in jewels in a frame. An insulated gold wire tip contained in the head of the slim tube, which supports the frame, terminates 0.1 mm from the blade tips. When the propeller revolves by the movement of a liquid past the blades, the passage of a blade past the gold wire tip slightly varies the measurable impedance between the tip and the tube. The variation of the impedance is amplified and it generates an electric pulse.

The calibration of the propeller probe (see Appendix II) shows that the inertia and the friction of the propeller are small enough so that the propeller can trace an alternating flow of 3.0 seconds period. In addition, the propeller is sensitive only to the velocity component which is parallel to the propeller spindle. Thus, the propeller probe has a good dynamic response to the wave motion with a period longer than 3.0 seconds. Though the response of the propeller to an alternating flow with shorter period than 3.0 seconds is not tested through calibration, it will be examined through the comparison of the results from the

propeller current meter with the measured velocity with the hot film anemometer in the periodic wave tests (Section 4.1).

3.3.2 TSI hot film probe (Photo 3.2)

The hot film probe has an orthogonal pair of quartz coated cylindrical hot film sensors with diameters of 0.006 inches (0.15 mm) and sensing lengths of 0.08 inches (2.0 mm). The space between the sensors is 0.04 inches (1.0 mm). The probe was operated at low overheating ratio (1.03) throughout the experiments in order to avoid the generation of air bubble on the sensor surface.

The hot film anemometer output is an analog voltage, E_B, functionally related to the flow speed, V, past the sensor as Eq. (2.15) or Eq. (2.16). For convenience in data processing, the output voltage, E_B, is linearized utilizing a TSI Model 1052 Linearizer. The linearizer approximates the non-linear relation between E_B and V by the following fourth order polynomial.

$$E = \sum_{i=1}^{4} C_i \left(E_B - E_0 \right)^i \qquad (3.1)$$

where E is the linearized output voltage and C_i's are the coefficients to be determined through calibrations.

Thus, the relation of the linearized output voltage to the flow speed is expressed as follows.

$$E = A(\theta)\, V \qquad (3.2)$$

where $A(\theta)$ is the directional coefficient for the linearized output voltage. The directional coefficient, $A(\theta)$, takes a maximum when the yaw angle, θ, is zero and decreases according to the increase of θ, up to 90

degree, but it is not a cosine function. This shows that the linearized output voltage does not give a true normal velocity component to the sensor axis unless θ is zero. As mentioned in Chapter 2, it is possible to reduce the horizontal and vertical velocity from the records obtained by simultaneous operation of an orthogonal pair of sensors if the directional coefficient $A(\theta)$ is determined correctly (13). However , because the main purpose of this experiment is to measure the maximum and minimum magnitude of the horizontal and vertical velocity components, the complete analysis of the velocity components is not done for this study.

The probe was installed so that sensor 1 (outer sensor) was vertical and sensor 2 (inner sensor) was horizontal. Thus, the former was most sensitive to the horizontal velocity component while the latter was most sensitive to the vertical velocity component. In the data reduction, the maximum values among the analog output voltage were processed using the calibration curve for $\theta = 0$.

The hot film probe and the support are shown in Fig. 3.4, and the sensor orientation is shown in Fig. 3.5. The calibration procedures and the results are described in detail in Appendix II.

4 RESULTS OF EXPERIMENTS

4.1 Periodic waves

4.1.1 Wave conditions

Periodic wave tests were conducted with the aim to examine the accuracy of Airy theory with the hot film anemometer when it is used to measure the horizontal and vertical velocity components. Both the hot film anemometer and the propeller current meter were operated simultaneously.

The wave conditions are listed in Table 4.1. These conditions reflect those listed in the reference(24) and cover a wide range of wave periods and wave heights within the capacity of the wave generator. The water depth, h, was 11 feet (3.35 m) throughout the experiments.

4.1.2 Sample record

A sample of the records is shown in Photo 4.1. Those records are, from the top, water surface elevation, non-linear output from the hot film anemometer channel 1 (vertical sensor), non-linear output from channel 2 (horizontal sensor), linearized output from channel 1, linearized output from channel 2 and the output fron the propeller current meter.

4.1.2.1 Propeller current meter

It is obviously seen that the pulses are dense at a wave crest and trough. The maximum frequency, n, of the pulses was determined as the mean frequency over a period from 0.2 to 0.3 seconds under the wave crest and the wave trough. The maximum velocities were reduced by the following relation obtained from the calibration (Appendix II).

$$u \text{ or } w = 0.0190\ n + 0.0845 \qquad (4.1)$$

where the unit of u and w is feet per second.

4.1.2.2 Linearized output voltage from the hot film anemometer

The output voltage from the sensor 1 shows maxima at wave crests and troughs while that from the sensor 2 shows minima. In the same way, the output voltage from the sensor 2 shows maxima when the water surface crosses the still water level while that from the other sensor shows minima. Thus, the variations of the output voltage from the sensor 1 and the sensor 2 are respectively similar to that of the magnitude of the horizontal and the vertical velocity. However, it should be noted that the minimum output voltages are not zero, while wave theories predict that the minimum magnitude of each velocity component is zero. This should be caused by the effect of the tangential velocity component to the sensor axis.

It is said that the effective speed U_{eff} to cool a hot film sensor can be obtained from the relation(30)

$$U_{eff}^2 = u_n^2 + K^2 u_t^2 \ . \qquad (4.2)$$

where u_n is the normal velocity component to a sensor axis, u_t is the tangential velocity component and K is a value between 0.1 and 0.3 depending upon the magnitude of the flow speed.

Hence, the output voltages in Photo 4.1 are contributed by both normal and tangential velocity components. These two contributions can be illustrated as shown in Fig. 4.1. It is seen that the contribution of the tangential velocity is small or vanishes when the output voltage takes a maximum. The maximum velocities were reduced from the maximum output voltage using the corresponding calibration curves.

For the convenience of the expression, the following symbols are used to represent each maximum velocity.

u_+: horizontal velocity beneath a wave crest

u_-: horizontal velocity beneath a wave trough

w_+: vertical velocity when the water surface crosses the still water level upward

w_-: vertical velocity when the water surface crosses the still water level downward.

The hypothesis that the minimum output voltage was caused by the tangential velocity component was tested. The minimum voltage of each sensor was plotted as functions of the maximum tangential velocity (deduced from the maximum voltage from the other sensor) as shown in Figs. 4.2 and 4.3. It is seen that the minimum voltages E_{1min} and E_{2min} are linearly related to the magnitude of the maximum tangential velocities, w_+ and u_+. The relation are well expressed by the straight lines in these figures. The slope of these lines represent the directional coefficient $A(\theta)$ for $\theta = 90^\circ$ in Eq.(3.2). The ratio $A(90^\circ)/A(0^\circ)$ are consistent throughout the periodic wave tests (see Table 4.2).

As shown in Table 4.1. the water particle velocities were measured at the level of two feet (0.61 m) and four feet (1.22 m) below the still water level. In addition to these two levels, the velocities at the level of one foot (0.30 m) below the still water level were measured with the hot film anemometer for some wave conditions. These additional tests were conducted with the interest in the hot film response when the probe was exposed to the air during the passage of the wave troughs.

Figure 4.4 shows a sample of these tests. The output voltage from

both sensors suddenly become zero when the probe emerges out of water. They quickly recover as the probe submerges. The output voltages show almost the same maximum values and profile for each individual wave. This shows that the effect of the probe exposure in the air to the sensor sensitivity, such as air bubbles adhering to the sensor surface, was small. Thus, the hot film probe can be operated near the still water level.

4.1.3 Measured velocities

The results of the periodic wave tests are summarized in Table 4.3. In this table, the velocities calculated from Stokes' fifth order theory (15), Dean's Stream Function theory(16) and Airy theory are listed.

The horizontal and vertical maximum velocities measured with the propeller current meter, $u_{propeller}$ and $w_{propeller}$, are compared with those measured with the hot film anemometer, $u_{hot\ film}$ and $w_{hot\ film}$, as shown in Fig. 4.5 for each probe level, z. In the figure, the correlation coefficients of these measured velocities are shown. They are very close to 1.0 for all the cases. Hence, both the propeller and the hot film did function well. From the figure, it is seen that the velocities measured with the propeller current meter are smaller than those measured with the hot film anemometer. The difference may be caused by the method of data processing.

The frequency of the output pulses from the propeller current meter were averaged over from 0.2 to 0.3 seconds. Thus obtained maximum velocities may be smaller than the true maximum velocity, as more closely detected by the hot film anemometer.

4.1.4 Comparison with wave theories

As seen in Table 4.3, there are small differences among the theoritical values given by the wave theories. There is no practical difference between the velocities given by Stokes' fifth order theory and those given by Dean's Stream Function Theory. Hence, the measured velocities are compared with the velocity distribution given by Stokes' fifth order theory and Airy theory for the cases that the latter theory gives notably different results from the former. The comparison are shown in Fig. 4.6 through 4.14 for each wave condition. As a whole, the measured maximum velocities are very close to the theoritical velocity distributions.

The correlation coefficients of the measured velocity with the hot film anemometer and the theoritical velocities given by these two wave theories are also very close to 1.0 as shown in Table 4.4.

The mean and the standard deviation of the relative error, r_p, defined by Eq. (4.3) is summarized in Table 4.5.

$$r_p = \frac{(u_+)_{measured} - (u_+)_{theory}}{(u_+)_{theory}}, \text{ etc.} \qquad (4.3)$$

The prediction of the velocities with Stokes' fifth order theory yields almost the same means and standard deviations as the prediction with Airy theory. The means of the relative error show that the horizontal velocities beneath the wave crests are three to four percent smaller and those beneath the wave troughs and 10 to 20 percent larger than the theoretical predictions. On the other hand, the measured vertical velocities, in general, are smaller than the theoritical predictions for both w_+ and w_-. The standard deviations are varying from 0.1 to 0.2

at the level of -4 feet, and they are about 0.1 at the level of -2 feet.

It is interesting that the measured horizontal velocity beneath the wave crests, u_+, are smaller, and those beneath the wave troughs, u_-, are larger than the predicted velocity from Airy theory. This shows that the magnitude of u_+ is smaller than u_-, since Airy theory gives equal magnitude for both u_+ and u_-. This is clearly seen in the measured velocity in Table 4.3. This tendency is a remarkable contrast with the theoritical results given by Stokes' fifth order theory and Dean's Stream Function Theory.

Many studies discuss the horizontal velocity beneath the wave crests of finite amplitude waves. However, there are few studies which show the velocities beneath the wave troughs. The experimental results reported by Goda(9) show that the horizontal velocities beneath the wave crests are smaller than those beneath the wave troughs for the most cases under intermediate water conditions (h/T^2 is larger than 0.8 ft/sec^2), while the opposite results are obtained for shallow water conditions (h/T^2 is less than 0.6 ft/sec^2). Iwagaki and Sakai(13) showed the time variation of horizontal velocity was close to the higher order wave theory (Stokes' third order theory) rather than Airy theory, i.e. u_+ was larger than u_-. However, they measured only near bottom velocity and their test waves were relatively shallow water conditions (h/T^2 is less than 0.5 ft/sec^2).

These variations of the velocity characteristics may be caused by the following reason. The water particle orbits are ellipses of which the axes decrease according to the increase of the distance downward from the still water level. On the other hand, the wave theories approximate the velocity at the mean position of a water particle with the velocity on the orbit. A stationary probe does not trace the water particle.

Beneath the wave crests, it measures the orbital velocity at the top of the orbit, the center of which is below the probe. On the other hand, beneath the wave troughs, it measures the orbital velocity at the bottom of the orbit, the center of which is above the probe. For given water depth and wave height, the axes of the elliptical water particle orbits are larger as the distance away from the bottom increases. Therefore, the measured orbital velocity beneath the wave troughs may be larger than that beneath the wave crests.

In addition, there should be non-linear effects due to a large wave motion. That is the orbital velocity of a water particle may be actually larger beneath the wave crests than that beneath the wave troughs. Consequently, near breaking, the orbits are no longer closed ones. For detail discussion, the water particle velocities should be measured at various levels over an entire cycle of the wave motion rather than the maximum velocities.

Though there are some differences between the measured and the predicted velocities as mentioned above, again, they are generally less than 10 percent. The wave theory(either Stokes' fifth order theory, Dean's Stream Function Theory and Airy theory) provides good prediction of the velocities for the wave conditions in this study as seen in Table 4.5.

4.2 Random wave

4.2.1 Wave conditions

Two kinds of wave spectra were employed in the random wave tests. The water particle velocities were measured with the hot film anemometer at two feet and four feet below the still water level. The run designations are listed in Table 4.6. The random wave trains last about 160 seconds and they are composed of about 60 zero upcrossing waves. The zero upcrossing wave heights and periods were read with a scale from the record on oscillograph paper.

The relation between the heights and the periods of the zero upcrossing waves are plotted with dots in Fig. 4.15 (spectrum I) and Fig. 4.16 (spectrum II). As these figures show, spectrum I is composed of steeper waves than spectrum II and the range of the wave periods is about the same for both spectra. The wave conditions employed in the periodic wave tests are plotted with white circles in Fig. 4.15. They cover most of the conditions associated with the discrete waves of the random waves.

The probability density and the cumulative probability of the wave heights are shown in Fig. 4.17 and Fig. 4.18, respectively. They are fairly close to the Rayleigh distribution.

4.2.2 Wave spectrum

4.2.2.1 Computation of the wave spectrum

Direct Fourier transformation of the time series $\eta(t)$ extending from t_1 to t_2 was computed to give the raw estimate of the power spectral density function at a frequency f as given by the following formula (27).

$$G_X(f) = \frac{2}{t_2 - t_1} \left| X(f) \right|^2 \qquad (4.4)$$

where $\tilde{G}_x(f)$ is the raw estimate of the power spectral density at the frequency f, and X(f) is the Fourier transformation of the time series $\eta(t)$.

The Fourier transformation X(f) is calculated from Eq. (4.5).

$$X(f) = \int_{-\infty}^{\infty} \eta(t)\, e^{-j2\pi ft}\, dt \tag{4.5}$$

For the practical calculation for a discrete record $\eta(t_m)$, m = 1,2,3,..., N, at a time interval τ, Eq. (4.5) is rewritten into

$$X(f) = \tau \sum_{m=1}^{N} \eta(t_m) \left[\cos(2\pi fm\tau) - j \sin(2\pi fm\tau)\right]$$

$$= A(f) - j\, B(f) \tag{4.6}$$

where $$t_2 - t_1 = N\tau \tag{4.7}$$

$$A(f) = \tau \sum_{m=1}^{N} \eta(t_m) \cos(2\pi fm\tau) \tag{4.8}$$

$$B(f) = \tau \sum_{m=1}^{N} \eta(t_m) \sin(2\pi fm\tau)\,. \tag{4.9}$$

Hence, the raw estimate of the spectral density, $\tilde{G}_x(f)$ is calculated by

$$\tilde{G}_x(f) = \frac{2}{t_2 - t_1} \left[A(f)^2 + B(f)^2\right]\,. \tag{4.10}$$

The parameters employed in the practical computations are as follows.

N = 1546, τ = 0.1 sec and f = 0.2 through 1.4 sec^{-1} (at an interval 0.01 sec^{-1})

The raw estimates $\tilde{G}_x(f)$ are smoothed with the use of a boxcar function,

Eq. (4.11).

$$G_x(f_m) = \frac{1}{10}\left[G_x(f_{m-5}) + G_x(f_{m-4}) + \ldots\ldots + G_x(f_{m+4})\right] \qquad (4.11)$$

4.2.2.2 Comparison with the Bretschneider spectrum

The Bretschneider spectrum is given by the following formula for a fully developed sea (33).

$$S_{H2}(\omega) = 3.437\ \frac{\overline{H}^2}{\overline{\omega}}\left(\frac{\overline{\omega}}{\omega}\right)^5 e^{-0.675\left(\frac{\overline{\omega}}{\omega}\right)^4} \qquad (4.12)$$

where $\overline{\omega} = 2\pi/\overline{T}$

The Bretschneider spectrum implies the following relationship.

$$\overline{H}^2 = 8\overline{\eta^2(t)} = \int_0^\infty S_{H2}(\omega)\ d\omega \qquad (4.13)$$

This should be carefully distiguished from

$$\overline{\eta^2(t)} = m_0 = \int_0^\infty S_{\eta\eta}(f)\ df \qquad (4.14)$$

where m_0 is the zeroth moment of $S_{\eta\eta}(f)$ about the origin.

From these two equations, the Bretschneider spectrum, $S_{H2}(\omega)$ is transformed into the common expression of wave spectrum as follows.

$$\left[S_{\eta\eta}(f)\right]_{\text{Bretschneider}} = \frac{2\left[S_{H2}(\omega)\right]_{\text{Bretschneider}}}{8} \qquad (4.15)$$

Figures 4.19 and 4.20 show the comparison of the measured spectrum with Bretschneider spectrum. In the computation of Bretschneider spectrum, the parameter $\overline{\eta^2(t)}$ and $\overline{T}$ obtained from the time series $\eta(t)$ are used to give the values, $\overline{H}$ and $\overline{\omega}$, in Eq.(4.12). For both cases, the spectrum of the test random waves show a close similarity to the Bretschneider spectrum, though the measured spectrum has somewhat larger density in the

lower frequency range, and smaller density in the higher frequency range.

The parameters associated with the measured spectra are summarized in Table 4.7. The significant wave heights, $H_{1/3}$, the mean wave heights, $\overline{H}$, and the mean wave periods, $\overline{T}$, which were computed from the moments of the measured spectra (28), are close to those calculated from zero upcrossing wave readings.

4.2.3 Sample data of velocity measurement

Figure 4.21 shows a sample record. Generally, the maxima of the output voltage from the hot film sensor 1 (Ch. 1) appear beneath the wave crests and the troughs while the output voltage from the hot film sensor 2 (Ch. 2) shows its minima there. The maxima of Ch.2 apper when the water surface crosses the still water level while the output of Ch. 1 shows the minima there. These aspects are clearly seen for large waves,and have the same general characteristics as observed in the periodic wave tests. Thus, the maximum values of the horizontal and vertical velocity components can be measured in the same way as in the periodic wave tests.

5 ESTIMATION OF VELOCITIES IN RANDOM WAVES

5.1 Statistical estimation through spectrum analysis

On the basis of Airy theory (linear wave theory), the horizontal velocity and the vertical velocity at a location are given by the following complex functions.

$$\left.\begin{aligned} u(t) &= a\,\omega\,\frac{\cosh k(z+h)}{\sinh kh}\; e^{j(kx-\omega t)} \\ w(t) &= -ja\,\omega\,\frac{\sinh k(z+h)}{\sinh kh}\; e^{j(kx-\omega t)} \end{aligned}\right\} \quad (5.1)$$

while the water surface elevation is given by

$$\eta(t) = a\, e^{j(kx-\omega t)}\,, \quad (5.2)$$

where a is the amplitude of the surface elevation ($a = H/2$) and $\omega = 2\pi f = 2\pi/T$, with T the wave period. Hence, the relation of the horizontal and vertical velocity to the water surface elevation are written as

$$\left.\begin{aligned} u(t) &= R'_u(f)\,\eta(t) \\ w(t) &= R'_w(f)\,\eta(t)\,, \end{aligned}\right\} \quad (5.3)$$

where

$$\left.\begin{aligned} R'_u(f) &= 2\pi f\,\frac{\cosh k(z+h)}{\sinh kh} \\ R'_w(f) &= -2\pi j f\,\frac{\sinh k(z+h)}{\sinh kh}\,. \end{aligned}\right\} \quad (5.4)$$

The functions $R'_u(f)$ and $R'_w(f)$ are called the frequency response functions. For the given location, they are the functions of only frequency, not functions of time.

The velocities u(t) and w(t) are thus linearly related to the water surface elevation. There are the following interrelationships between the spectral density of the horizontal velocity, u(t), or the vertical velocity, w(t), and that of the surface elevation (31).

$$\left.\begin{aligned} S_{uu}(f) &= \left|R'_u(f)\right|^2 S_{\eta\eta}(f) \\ S_{ww}(f) &= \left|R'_w(f)\right|^2 S_{\eta\eta}(f) \end{aligned}\right\} \quad (5.5)$$

where $S_{uu}(f)$ is the spectral density of the horizontal velocity fluctuation and $S_{ww}(f)$ is the spectral density of the vertical velocity fluctuation. Utilizing the above two equations, the velocity spectra are estimated from a given wave spectrum.

Once the velocity spectra $S_{uu}(f)$ and $S_{ww}(f)$ are obtained, the probability density of maximum velocities and the mean interval of zero upcrossings associated with the random variation of the velocities, with the use of the following equation presented by Cartwright and Longuet-Higgins (28).

i) Probability density of maxima

$$p(x_m) = \frac{1}{\sqrt{2\pi m_0}}\left[\varepsilon \exp\left(-\frac{x_m^2}{2\varepsilon m_0}\right) + (1-\varepsilon^2)^{\frac{1}{2}}\frac{x_m}{\sqrt{m_0}}\exp\left(-\frac{x_m^2}{2m_0}\right)\int_{-\infty}^{\frac{x_m}{\sqrt{m_0}}(1-\varepsilon^2)^{\frac{1}{2}}/\varepsilon}\exp\left(-\frac{x^2}{2}\right)dx\right] \quad (5.6)$$

where $p(x_m)$ is the probability density of x_m, x_m is the maximum values of random function x(t), ε is the spectral width defined as

$$\varepsilon^2 = \frac{m_0 m_4 - m_2^2}{m_0 m_4} \quad (5.7)$$

and m_ν is the νth moment of the spectrum about the origin, i.e.

$$m_\nu = (2\pi)^\nu \int_0^\infty f^\nu S_{xx}(f)\, df \tag{5.8}$$

where $S_{xx}(f)$ is the spectral density function of $x(t)$.

ii) Mean interval of zero upcrossing

$$\bar{T} = 2\pi(m_0/m_2)^{\frac{1}{2}} \tag{5.9}$$

Figures 5.1 and 5.2 show velocity spectra from the operation of Eq. (5.5) for the horizontal and vertical velocity, respectively. The response functions $R'_u(f)$ and $R'_w(f)$ are also plotted on these figures. The frequency response functions $R'_u(f)$ and $R'_w(f)$ behave as filters which attenuate the contribution of wave spectrum $S_{\eta\eta}(f)$ to velocity spectra $S_{uu}(f)$ and $S_{ww}(f)$ for the higher frequency range, and which amplify it for the frequency range about the peak of $S_{\eta\eta}(f)$. The resultant velocity spectra thus become narrower banded spectra than the wave spectra.

The band width of a spectrum is characterized by a parameter, ε, which is calculated from Eq. (5.7). The parameter ε of the computed velocity spectra and zeroth, second and fourth moments of it are listed in Table 5.1 for spectrum I and in Table 5.2 for spectrum II. These tables show that the spectral widths fall within the range from 0.4 to 0.5 while the spectral width of the wave spectrum is about 0.65 for both spectra. The former is obviously smaller than the latter.

For a value of ε smaller than 0.5, the probability density, Eq.(5.6), is very close to the Rayleigh distribution, which corresponds to the case $\varepsilon = 0$. As a matter of fact, the probability distribution of the measured maxima of the horizontal velocity shows good agreement with the Rayleigh distribution as shown in Fig. 5.3.

Thus, the probability distribution of the maximum velocity can be approximated by the Rayleigh distribution:

$$P(u_{max}) = \frac{u_{max}}{m_0} \exp(- u_{max}^2 /2m_0). \tag{5.10}$$

This distribution yields the following relations among characteristic values of u_{max} (28).

$$\begin{aligned} u_{1/10} / \sqrt{m_0} &= 2.55 \\ u_{1/3} / \sqrt{m_0} &= 2.0 \\ \bar{u} / \sqrt{m_0} &= 1.25 \end{aligned} \tag{5.11}$$

where $m_0 = \overline{u^2(t)}$.

These theoretical results are summarized together with the experimental results as listed in Table 5.3.

Consider the relative error of the statistical velocity estimates by the following definition:

$$r_s = \frac{(u_{1/\ell})_{measured} - (u_{1/\ell})_{predicted}}{(u_{1/\ell})_{predicted}} \tag{5.12}$$

where $u_{1/\ell}$ is the mean of one-ℓth largest maximum velocities. The relative errors calculated from the values in Table 5.3 are plotted on Fig. 5.4 for each run. The range of the relative error is from -0.2 to 0.2.

5.2 Estimation by simple application of periodic wave theory

In this section, the relation of discrete waves in random wave to a theoretical periodic wave model is examined from the view point of the maximum water particle velocities.

5.2.1 Theoretical wave model

As discussed in Chapter 4.2 and compared in Table 4.3, for the level -2 and -4 feet and the test wave conditions, the maximum velocities predicted from Airy theory are very close to those predicted from the higher order wave theories: Stokes' fifth order theory and Dean's Stream Function theory*. In addition, as compared in Table 4.6, there is no practical difference in the means and the standard deviation of the relative error, r_p, whichever theory is used to predict the maximum velocities.

Thus, Airy theory gives a good approximation to the higher order theories. Hence, for the convenience of the computation, Airy theory is used to predict velocities of each discrete waves in a random wave train.

5.2.2 Prediction of velocity

From each zero upcrossing wave height and period, the maximum velocities at the level z are calculated as follows with the aid of Airy theory.

$$\left.\begin{aligned} (u_{predicted})_i &= \left|R'_u(f_i)\right| H_i/2 \\ (w_{predicted})_i &= \left|R'_w(f_i)\right| H_i/2 \end{aligned}\right\} \quad (5.13)$$

where $f_i=1/T_i$, and H_i and T_i are zero upcrossing wave height and period of ith wave.

---

* This does not imply that the velocities predicted by Airy theory are close to those predicted by the higher order theories over an entire cycle of the wave motion. Above discussion holds only for the maximum velocities.

The correlation of thus predicted velocities and the observed velocities of the discrete waves are shown in Figs. 5.5 and 5.6. for the case of spectrum I at the level z = -2 feet. Figure 5.5 shows the correlation of the horizontal velocities, and Fig. 5.6 shows the correlation of the vertical velocities. As seen in these figures, the relations between the observed and the predicted velocities of the discrete waves widely scatter. Among the four maximum velocities, u_+, u_-, w_+, w_-, the extent of the scattering is relatively small for w_-.

The large scattering is probably from the asymmetric water surface profile about the still water level. One asymmetry is the nonlinear wave profile which is characterized by a steep crest and a flat trough. Another is caused by the irregularity of the water surface fluctuation, i.e. the fact that large crests are not always followed by large troughs and small crests are not always followed by small troughs.

As examined in the previous chapter, the effect due to the asymmetry is supposed to be small. Hence, the difference between the observed and and predicted velocities is mainly caused by the asymmetry of the wave profile due to the irregular water surface motion.

The extents of the scattering are quantitatively expressed by correlation coefficients. The correlation coefficients for all the runs are summarized as shown in Table 5.4, together with the coefficients, a and b, of the linear regression equation (5.14) computed by least-squares method.

$$(u_+)_{observed} = a\,(u_+)_{predicted} + b \text{ , etc.} \qquad (5.14)$$

From Table 5.4, the correlation coefficients of u_+ and u_- are almost

equvalent and they are ranging from 0.8 to 0.9. The correlation coefficients of w_+ and w_- show a contrast. That is, the coefficients of w_+ are about 0.6 for most cases while those of w_- are about 0.9.

Such a difference results from the definition of the wave height and period which are used to predict the vertical velocities. The maximum velocity w_- is observed within a zero upcrossing wave. On the other hand, w_+ is observed inbetween two adjacent zero upcrossing waves. Therefore, the zero upcrossing wave heights and periods (crest to trough height and period) are suitable to characterize the wave associated with w_-, but they are not a direct parameter to characterize the wave associated with w_+. Some other definition of wave height and period may provide a closer prediction of w_+. Possibilities are trough to crest height and mean of the zero upcrossing wave height and period fore and aft the zero upcrossing.

Regardless of the scattering due to the irregularity of the random wave motion, the linear regression lines are, in general, close to the relation:

$$(u_+)_{observed} = (u_+)_{predicted}, \tag{5.15}$$

i.e. a = 1.0 and b = 0, approximately.

5.2.3 Probability of error

The observed maximum velocities are random veriables. The predicted ones are also random variable, since they are given as the functions of two random variable: zero upcrossing wave height and period. The relative error which is defined by Eq. (5.16) is thus a random variable.

$$r_D = \frac{(u_+)_{observed} - (u_+)_{predicted}}{(u_+)_{predicted}} \quad , \text{etc.} \tag{5.16}$$

The distribution of the relative error is plotted on a normal probabilty paper for several sample populations taken from a train of 64 to 70 waves: populations of one-tenth, one-third, one-half, two-thirds and nine tenths highest waves. Some examples are shown in Fig. 5.7 through Fig.5.10. The distribution for each population is well expressed by a straignt line on the normal probability paper.

The error distributions of other populations are not shown in the figures. However, almost all sample populations, except some population which include small waves, passed the Chi square test (32) at the significant level of 95 % as shown in Table 5.5. Because of the small sample size, Chi square tests are not done for the population of one-tenth highest waves. Thus, the distribution of the relative error is normal.

It is easily seen in Fig. 5.7 through Fig. 5.10 that the slopes of the distribution for one-tenth and one-third highest waves are steeper than those for others. This shows that the standard deviations of relative error for the "large wave" populations are smaller than those for the "small wave" populations. The mean and the standard deviation of the relative error for each population is summarized in Figs. 5.11 through 5.14. It is seen for all the cases that the standard deviations for "large wave" population are smaller than those for the population including small waves. In addition, the standard deviations for one-tenth and one-third highest waves are almost comparative to the standard deviations of the relative errors for periodic waves (see Table 4.5).

Note that the design wave is a large wave.

The means of the relative errors fall within the range from -2.0 to 0.2. This range is about twice of the range observed for periodic waves

(see table 4.5), and the same range as seen in the statistical estimation, Fig. 5.4. In addition, some similar aspects of the mean relative error are observed between Figs. 5.11 to 5.14 and Table 4.5:

For many cases, the mean relative error for u_+ is negative while that for u_- is positive. The mean relative errors for $w_+$and w_- are generally negative. This shows that the measured u_+ is smaller than the predicted u_+. On the other hand the measured u_- is larger than the predicted one. The measured w_+ and w_- are smaller than the predicted ones. Thus, the deviation of the mean relative error from zero results from the error associated with the wave theory.

The above discussion is summarized as follows.

The mean of maximum velocities of one-tenth, one-third,etc., highest waves can be well estimated by fitting proper periodic waves to the zero upcrossing wavs. The realizations of maximum velocities are normally distributed about the means, i.e. the predicted maximum velocities. The standard deviations of the relative error which is defined by Eq. (5.16) are small for large waves in a random wave train: the standard deviations associated with u_+, u_-, and w_- are less than 0.3 for one-third highest waves, and are less than 0.2 for one-tenth highest waves.

6 CONCLUSIONS

Summimng up the results of the study described above, the following are the major conclusions.

6.1 Periodic wave tests

1. The maximum horizontal and vertical velocities can be measured accurately with a hot film anemometer. The correlation between the maximum velocities measured with the hot film anemometer and those measured with the propeller current meter was quite good.

2. For deep water waves and near deep water wave conditions, i.e. h/T^2 is larger than 0.51, and within the range where H/H_b is smaller than 0.75, Stokes' fifth order theory, Dean's Stream Function Theory and Airy theory give good predictions of the maximum velocities. The mean and the standard deviation of the relative error defined by Eq. (4.3), turned out to be almost the same values whichever theory was used to predict the maximum velocities. This shows that Airy theory is no worse than the other two higher order wave theories for the prediction of the maximum velocities below wave troughs.

3. For most cases, the magnitude of the measured horizontal velocity beneath the wave troughs are larger than those beneath the wave crests. Such a tendency detected by the stationary probe may due to the characteristics of deep water waves.

6.2 Random wave tests

1. The spectrum analyses give a good statistical estimation of the maximum velocities at the level below the wave troughs. The relative errors are less than 10 percent for most cases.

2. The maximum velocities of discrete zero upcrossing waves can be predicted by fitting appropriate periodic waves to the zero upcrossing waves. The measured maximum velocities widely scatter about the above predicted velocities. However, the relation between the measured and the predicted maximum velocities obtained by the least-squares method turned out to be close to the relation:

$$(u_+)_{measured} = (u_+)_{predicted}, \text{ etc.} \tag{6.1}$$

3. The relative errors defined by Eq.(5.16) are normally distributed. The characteristics of the mean relative errors are similar to the characteristics of the relative error for periodic waves. Hence, the deviation of the relative error from zero is partly caused by the error introduces by the wave theory.

4. The relative errors are smaller for "large wave" populations than those for "small wave" populations.

5. Design waves are large waves. Thus, the results may make engineers confident when they use periodic wave theory to estimate the maximum velocities of the design wave.

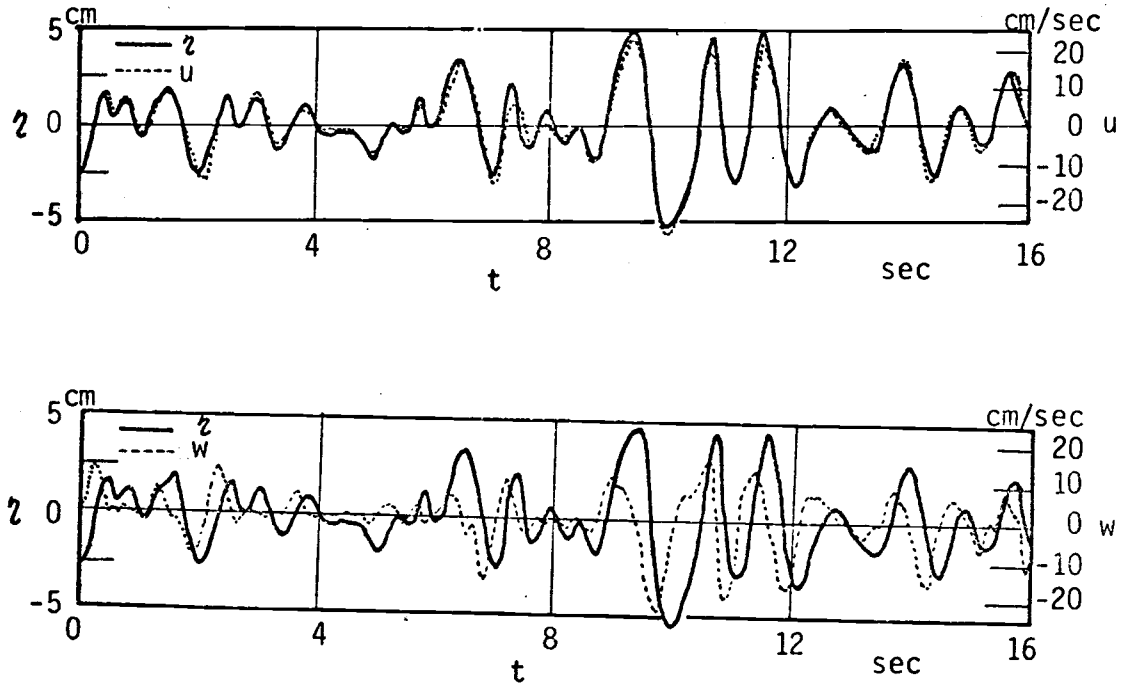

Fig. 2.1 Measured surface elevation and velocities of random wave
(after Iwagaki, Sakai and Ishida, 1973)

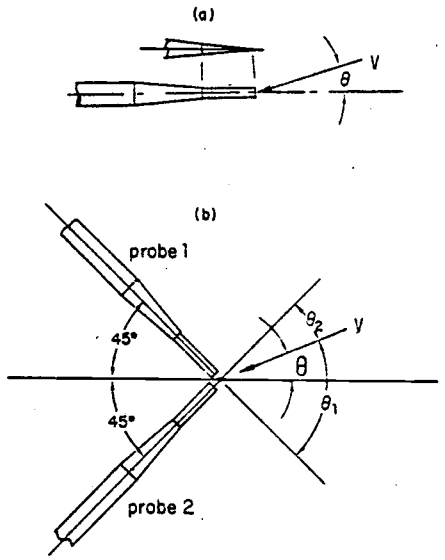

Fig. 2.2 (a) single, and (b) orthogonal
hot film probe geometry.
(after Van Dorn, 1975)

Table. 2.1 Velocity factor α

h/L_A	0.03	0.05	0.07	0.10	0.14	0.20	0.30	0.50	0.70
α	1.50	1.50	1.43	1.25	0.97	0.68	0.49	0.25	0.27

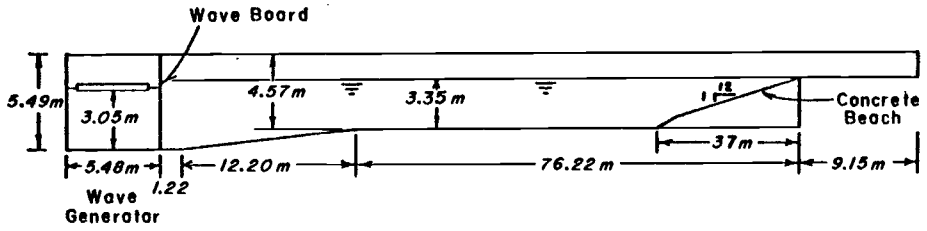

Fig. 3.1 General view of wave tank

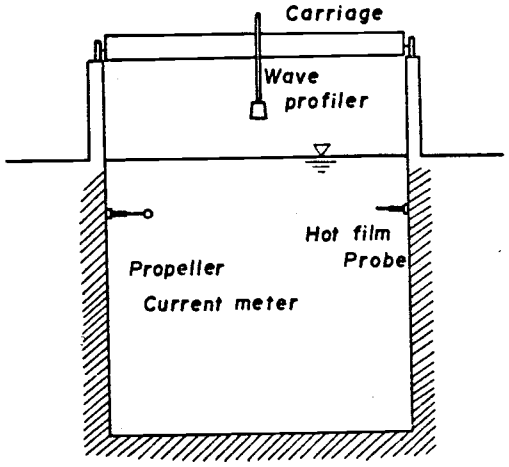

Fig. 3.2 Probe set up (looking from the wave board)

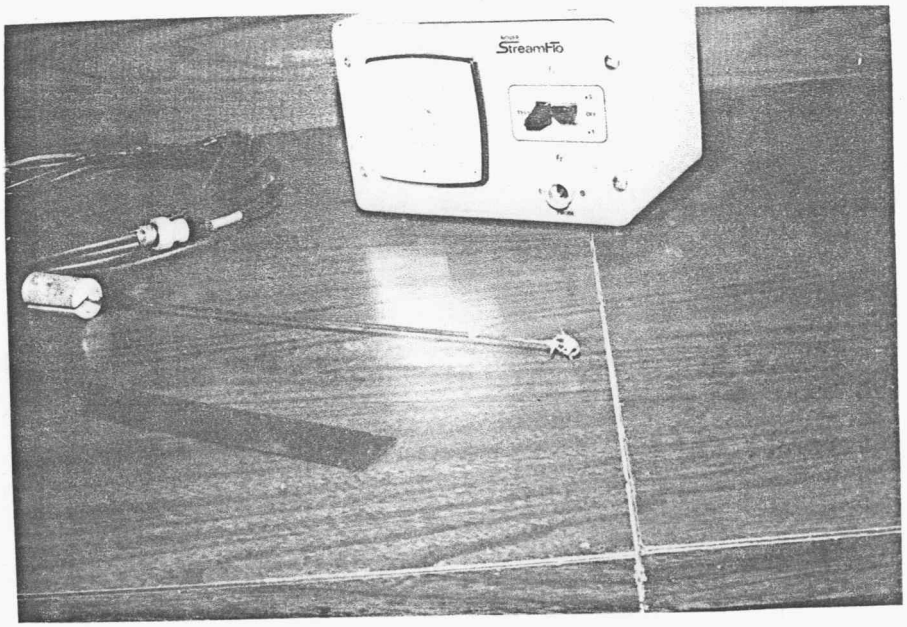

Photo 3.1 Propeller probe

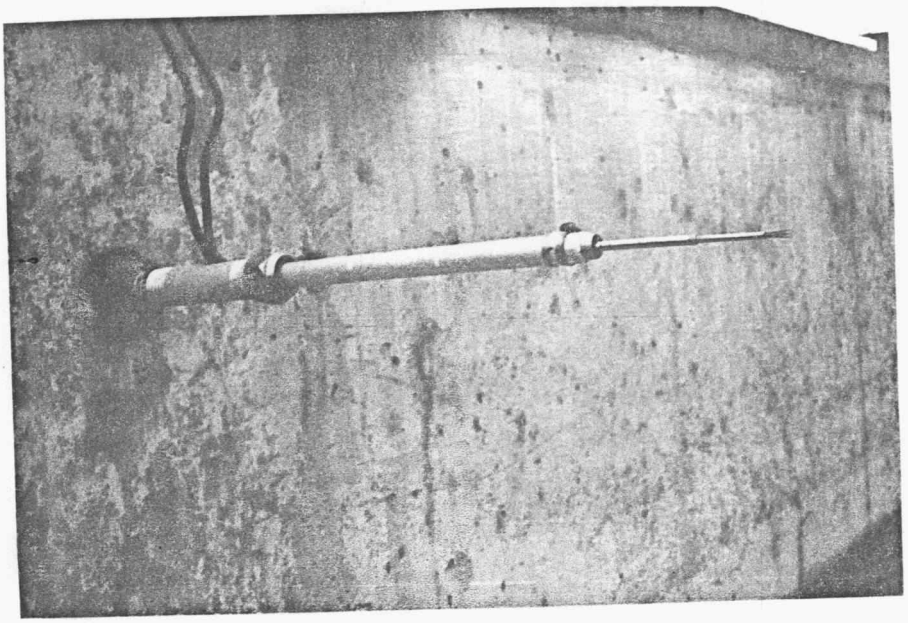

Photo 3.2 Hot film probe

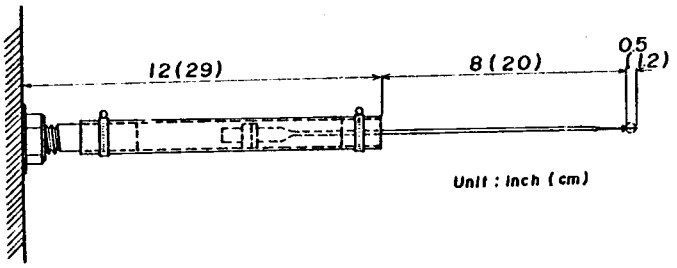

Fig. 3.3 Propeller probe and support

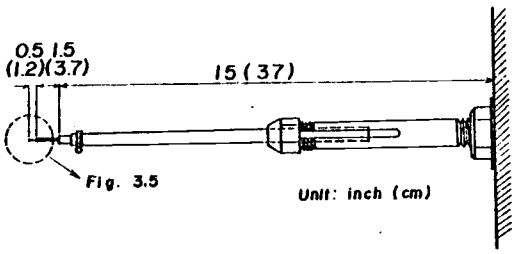

Fig. 3.4 Hot film probe and support

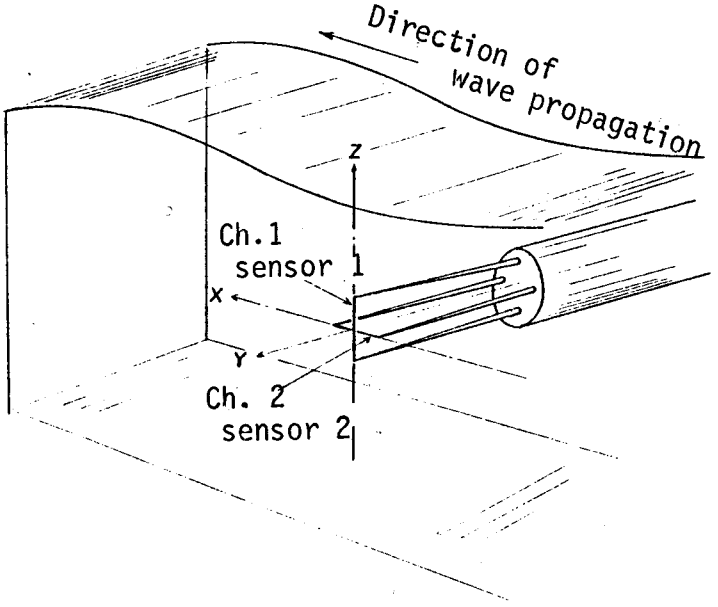

Fig. 3.5 Sensor orientation

Table 4.1 Run designation

Series	Run	Probe position: Hot film z ft(m)	Probe position: propeller z	Probe position: propeller Direction	Wave hight ft (m)	Wave period sec	Hot film calibration u_+	Hot film calibration u_-	Hot film calibration w_+	Hot film calibration w_-	Index Ref.(24)
I	H-1	-4(1.22)	-4	Hori-	3.61(1.10)	2.50	2	1	5	5	
	H-2			zontal	1.62(0.49)	2.50					
	H-3				2.71(0.83)	2.07					8-C
	H-4				0.94(0.29)	2.07					8-A
	H-5				1.33(0.41)	1.47					9-C
	H-6				0.47(0.14)	1.47					9-A
	H-7				2.01(0.61)	4.65					6-A
	H-8				1.72(0.52)	3.28					7-A
	H-9				3.44(1.05)	3.28					7-C
	V-1	-4(1.22)	-4	Ver-	3.61(1.10)	2.50	4	3	6	6	
	V-2			tical	1.62(0.49)	2.50					
	V-3				2.71(0.83)	2.07					8-C
	V-4				0.94(0.29)	2.07					8-A
	V-5				1.33(0.41)	1.47					9-C
	V-6				0.47(0.14)	1.47					9-A
	V-7				2.01(0.61)	4.65					6-A
	V-8				1.72(0.52)	3.28					7-A
	V-9				3.44(1.05)	3.28					7-C
II	H-1	-2(0.61)	-2	Hori-	3.61(1.10)	2.50	8	7	9	9	
	H-2			zontal	1.62(0.49)	2.50					
	H-3				2.71(0.83)	2.07					8-C
	H-4				0.94(0.29)	2.07					8-A
	H-5				1.33(0.41)	1.47					9-C
	H-6				0.47(0.14)	1.47					9-A
	H-7				2.01(0.61)	4.65					6-A
	H-8				1.72(0.52)	3.28					7-A
	H-9				3.44(1.05)	3.28					7-C
	V-1	-2(0.61)	-2	Ver-	3.61(1.10)	2.50	8	7	10	10	
	V-2			tical	1.62(0.49)	2.50					
	V-3				2.71(0.83)	2.07					8-C
	V-4				0.94(0.29)	2.07					8-A
	V-5				1.33(0.41)	1.47					9-C
	V-6				0.47(0.14)	1.47					9-A
	V-7				2.01(0.61)	4.65					6-A
	V-8				1.72(0.52)	3.28					7-A
	V-9				3.44(1.05)	3.28					7-C

Water depth h = 11 feet (3.35 m)

Calibration curves (unit: u,w ft/sec, E: volt)

1	u=0.395E	2	u=0.425E
3	u=0.427E	4	u=0.517E
5	w=0.458E	6	w=0.526E
7	u=0.448E	8	u=0.484E
9	w=0.363E	10	w=0.407E

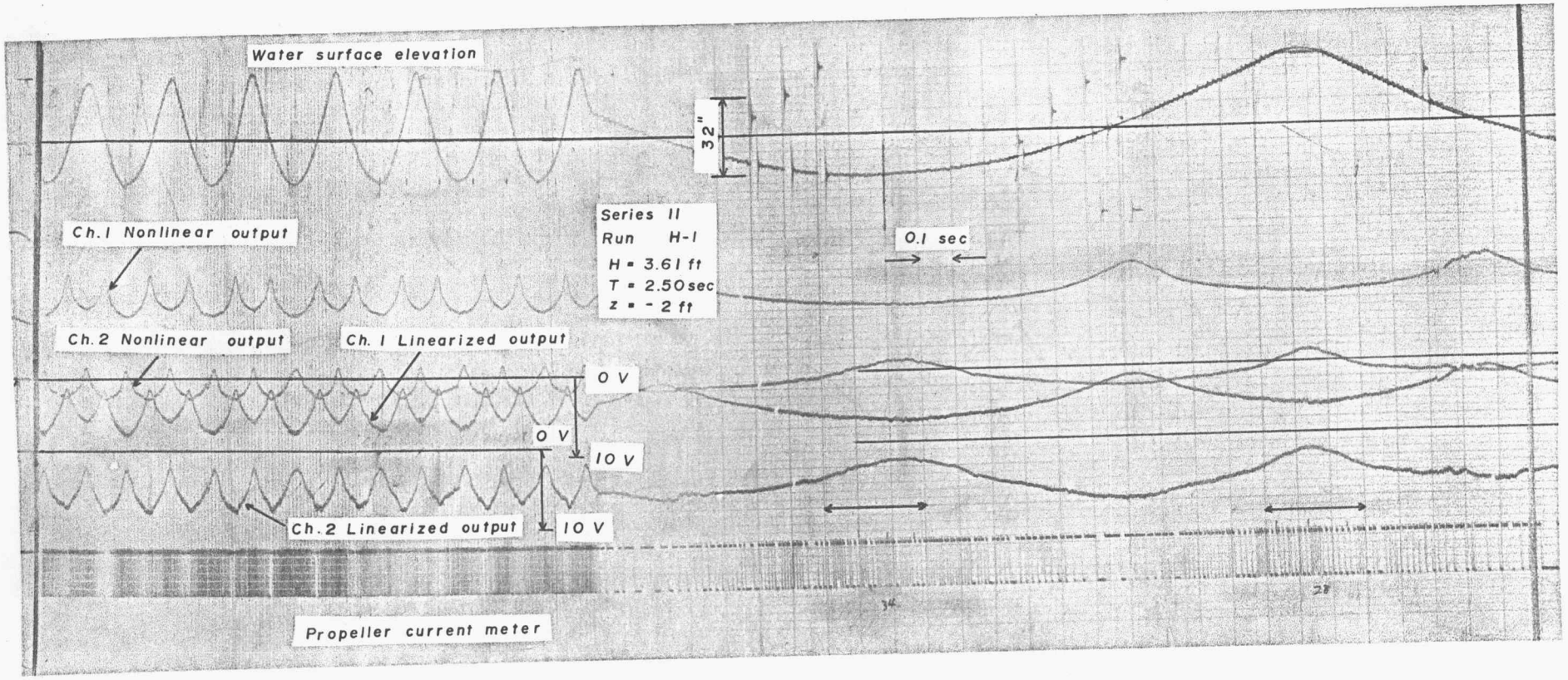

Photo 4.1 Sample record

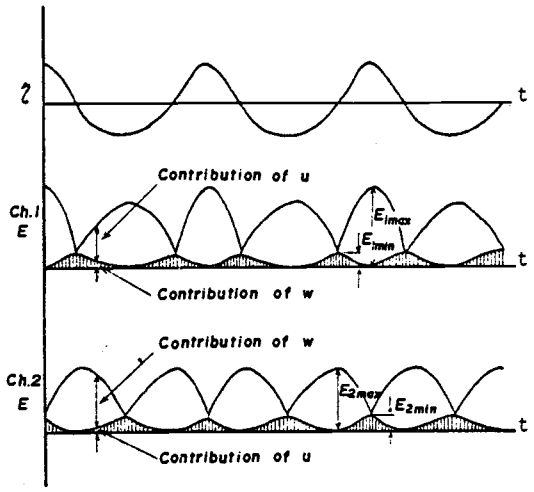

Fig. 4.1 Illustration of linearized out put voltage

Table-4.2 Directional coefficient $A(\theta)$

Series	Sensor	$A(0°)$*	$A(90°)$**	$A(0°)/A(90°)$
I	Vertical sensor	2.07	0.57	0.27
	Horizontal sensor	2.76	0.82	0.30
II	Vertical sensor	2.35	0.64	0.27
	Horizontal sensor	2.18	0.60	0.28

* obtained from the calibration

** obtained from Fig.-4.2 and 4.3

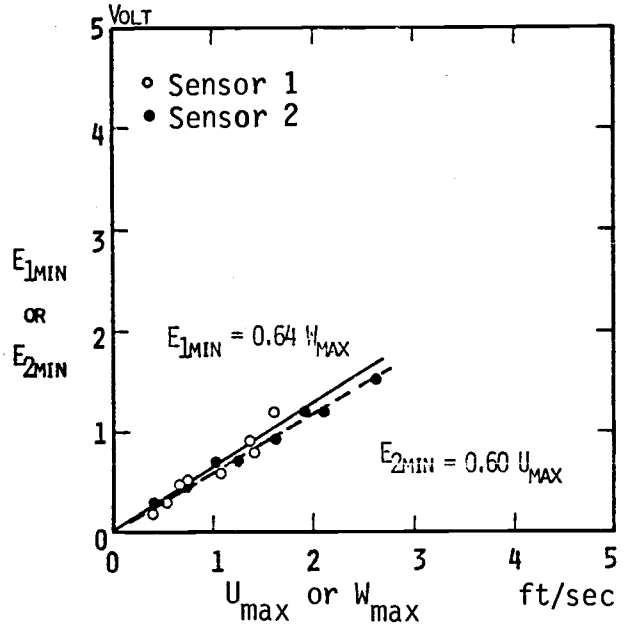

Fig. 4.2 Hot film sensitivity to tangential velocity (z=-4 ft)

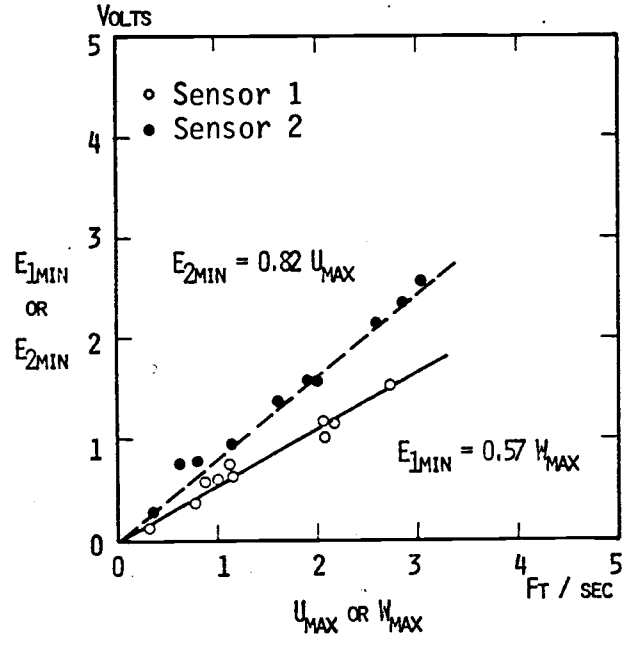

Fig. 4.3 Hot film sensitivity to tangential velocity (z=-2 ft)

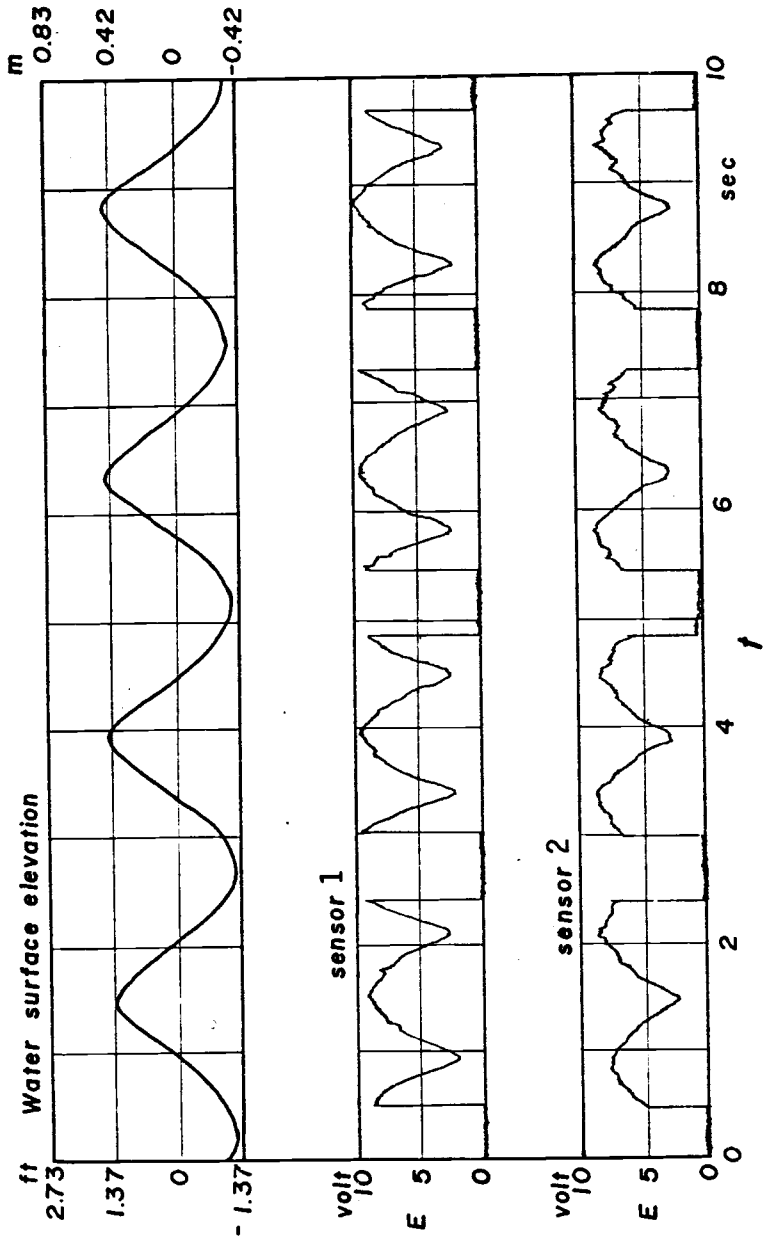

Fig. 4.4 Sample record (z=-1 ft, H=2.74 ft, T=2.50 sec)

Table 4.3 Results of data reduction and theoretical values (ft/sec)

Series	Run	Measurement								Theory								Run
		Hot film				Propeller				Stokes 5th			Stream Funct.			Airy		
		u_+	u_-	w_+	w_-	u_+	u_-	w_+	w_-	u_+	u_-	w	u_+	u_-	w	u	w	
I	H-1	1.91	2.31	1.58	1.58	1.60	2.37			2.17	2.02	1.77				2.19	1.91	H-1
	H-2	0.83	0.94	0.53	0.68	0.85	0.78			0.76	0.75	0.65				0.76	0.67	H-2
	H-3	1.19	1.56	1.00	1.00	1.05	1.38			1.36	1.31	1.23	1.37	1.31	1.23	1.35	1.28	H-3
	H-4	0.47	0.57	0.47	0.47	0.54	0.49			0.46	0.46	0.43	0.46	0.46	0.43	0.46	0.44	H-4
	H-5	0.36	0.47	0.21	0.37	—	—			0.34	0.33	0.33	0.36	0.35	0.34	0.36	0.34	H-5
	H-6	0.10	0.09	0.08	0.08	—	—			0.11	0.11	0.11	0.11	0.11	0.11	0.11	0.11	H-6
	H-7	1.81	1.46	0.63	0.63	1.53	1.32			1.68	1.41	0.80	1.68	1.41	0.80	1.58	0.79	H-7
	H-8	1.45	1.32	0.79	0.79	1.18	1.15			1.25	1.18	0.84	1.25	1.18	0.85	1.22	0.86	H-8
	H-9	2.59	2.55	1.74	1.74	2.17	2.42			2.48	2.12	1.64	2.47	2.18	1.63	2.45	1.73	H-9
	V-1	1.91	2.09	1.65	1.83			1.66	1.51	2.17	2.02	1.77				2.19	1.91	V-1
	V-2	0.68	0.79	0.55	0.64			0.67	0.58	0.76	0.75	0.65				0.76	0.67	V-2
	V-3	1.02	1.50	1.15	1.15			0.66	1.09	1.36	1.31	1.23	1.37	1.31	1.23	1.35	1.28	V-3
	V-4	0.42	0.51	0.37	0.46			0.37	0.47	0.46	0.46	0.43	0.46	0.46	0.43	0.46	0.44	V-4
	V-5	0.17	0.39	0.23	0.32			—	—	0.34	0.33	0.33	0.36	0.35	0.34	0.36	0.34	V-5
	V-6	0.17	0.12	0.18	0.09			—	—	0.11	0.11	0.11	0.11	0.11	0.11	0.11	0.11	V-6
	V-7	1.66	1.38	0.73	0.60			0.80	0.81	1.68	1.41	0.80	1.68	1.41	0.80	1.58	0.79	V-7
	V-8	1.23	1.14	0.69	0.69			0.88	0.81	1.25	1.18	0.84	1.26	1.18	0.85	1.22	0.86	V-8
	V-9	2.12	2.09	1.28	1.42			1.54	1.60	2.48	2.12	1.64	2.47	2.18	1.63	2.45	1.73	V-9

Table 4.3 Results of data reduction and theoretical values (ft/sec) continued

Series	Run	Measurement								Theory								Run
		Hot film				Propeller				Stokes 5th			Stream Funct.			Airy		
		u_+	u_-	w_+	w_-	u_+	u_-	w_+	w_-	u_+	u_-	w	u_+	u_-	w	u	w	
II	H-1	2.52	2.87	2.58	2.58	2.23	2.17			3.05	2.67	2.66				3.17	2.95	H-1
	H-2	1.16	1.34	0.91	0.91	0.97	1.12			1.10	1.08	1.01				1.11	1.03	H-2
	H-3	2.03	2.46	2.18	2.18	1.85	2.10			2.25	2.12	2.09	2.25	2.11	2.09	2.35	2.29	H-3
	H-4	0.77	0.99	0.80	0.80	0.81	0.80			0.81	0.81	0.77	0.80	0.79	0.76	0.81	0.79	H-4
	H-5	0.82	1.03	0.91	0.73	0.68	0.85			0.94	0.91	0.90	0.98	0.94	0.93	0.94	0.93	H-5
	H-6	0.34	0.45	0.33	0.30	0.28	0.37			0.33	0.33	0.32	0.33	0.33	0.32	0.34	0.33	H-6
	H-7	1.94	1.97	1.09	0.80	1.60	1.79			1.87	1.51	1.07	1.87	1.51	1.07	1.73	1.05	H-7
	H-8	1.50	1.79	1.09	1.09	1.35	1.30			1.52	1.42	1.18	1.52	1.42	1.18	1.46	1.20	H-8
	H-9	2.76	3.09	2.21	2.21	2.54	2.61			3.04	2.54	2.29	3.03	2.56	2.28	2.98	2.41	H-9
	V-1	2.52	2.73	2.89	2.89			2.03	2.73	3.05	2.67	2.66				3.17	2.95	V-1
	V-2	1.16	1.34	1.26	1.10			1.03	1.00	1.10	1.08	1.01				1.11	1.03	V-2
	V-3	2.18	2.33	2.20	2.20			2.10	1.84	2.25	2.12	2.09	2.25	2.11	2.09	2.35	2.29	V-3
	V-4	0.97	0.99	0.90	0.73			0.87	0.72	0.81	0.81	0.77	0.80	0.79	0.76	0.81	0.79	V-4
	V-5	0.87	0.94	0.90	0.77			0.66	0.47	0.94	0.91	0.90	0.98	0.94	0.93	0.94	0.93	V-5
	V-6	0.34	0.40	0.45	0.37			0.32	0.36	0.33	0.33	0.32	0.33	0.33	0.32	0.34	0.33	V-6
	V-7	1.79	1.88	1.10	0.85			1.00	0.99	1.87	1.51	1.07	1.87	1.51	1.07	1.73	1.05	V-7
	V-8	1.50	1.75	1.22	1.22			1.13	1.21	1.52	1.42	1.18	1.52	1.42	1.18	1.46	1.20	V-8
	V-9	2.18	3.18	2.48	2.48			2.29	2.39	3.04	2.54	2.29	3.03	2.56	2.28	2.98	2.41	V-9

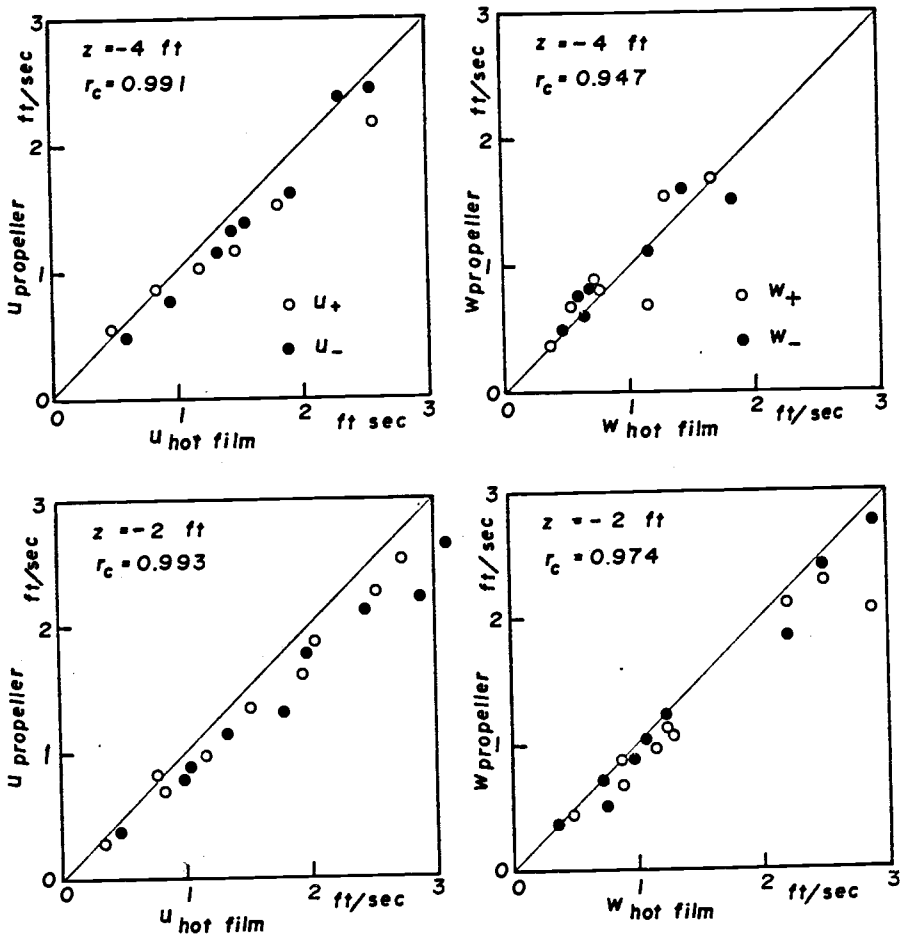

Note: The correlation coefficient of variavles x and y is defined as

$$r_c = \frac{\Sigma\{(x-\bar{x})(y-\bar{y})\}}{\sqrt{\{\Sigma(x-\bar{x})^2\}\{\Sigma(y-\bar{y})^2\}}} .$$

Fig. 4.5 Correlation of the measured velocities with propeller with those measured with hot film

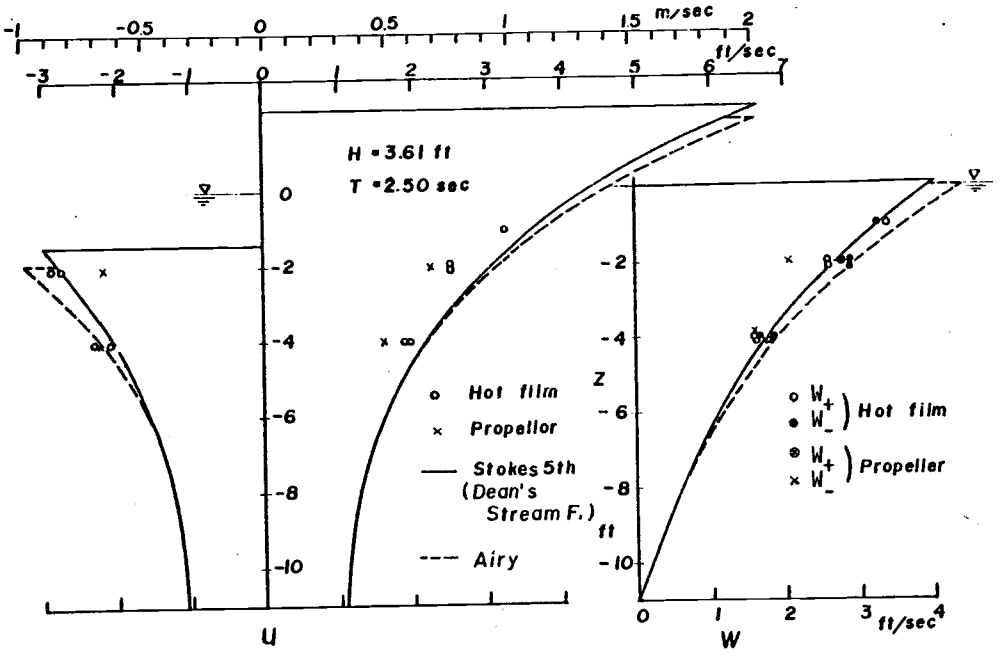

Fig. 4.6 Comparison with theory (Run 1)

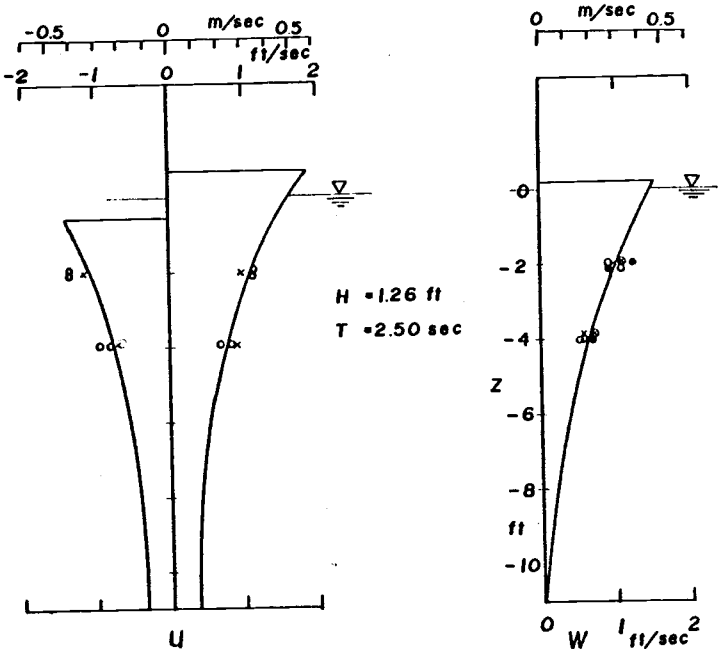

Fig. 4.7 Comparison with theory (2)

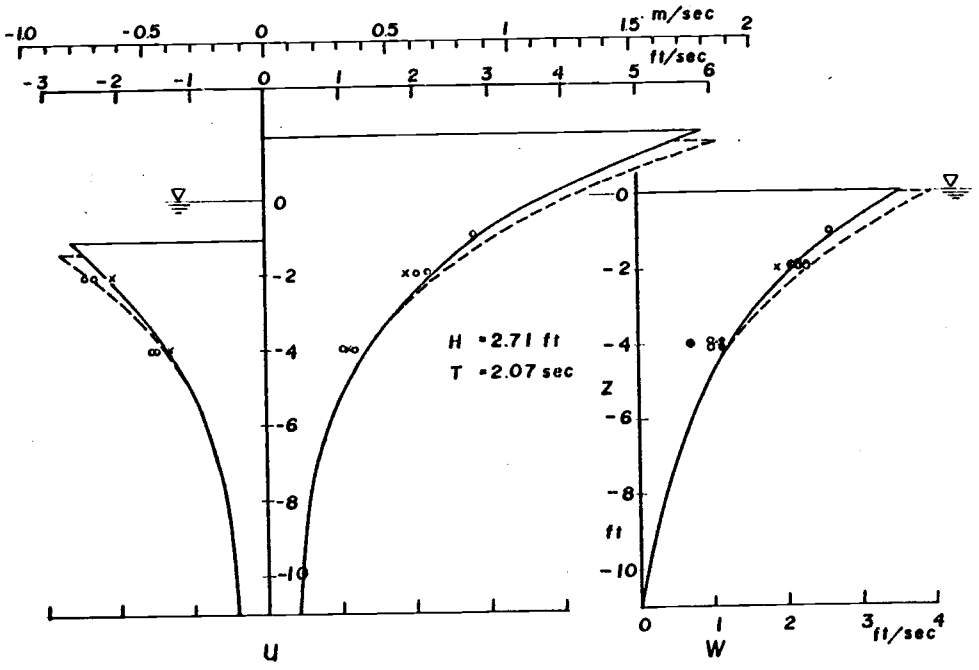

Fig. 4.8 Comparison with theory (3)

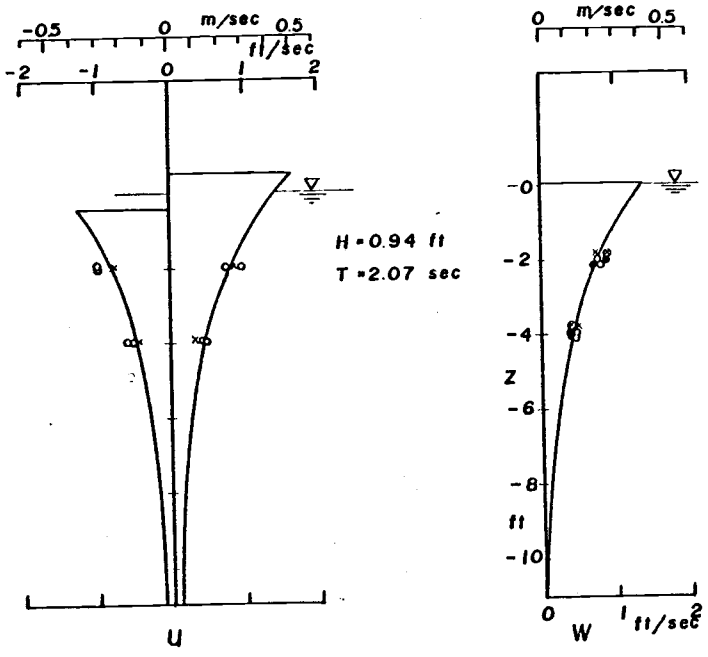

Fig. 4.9 Comparison with theory (4)

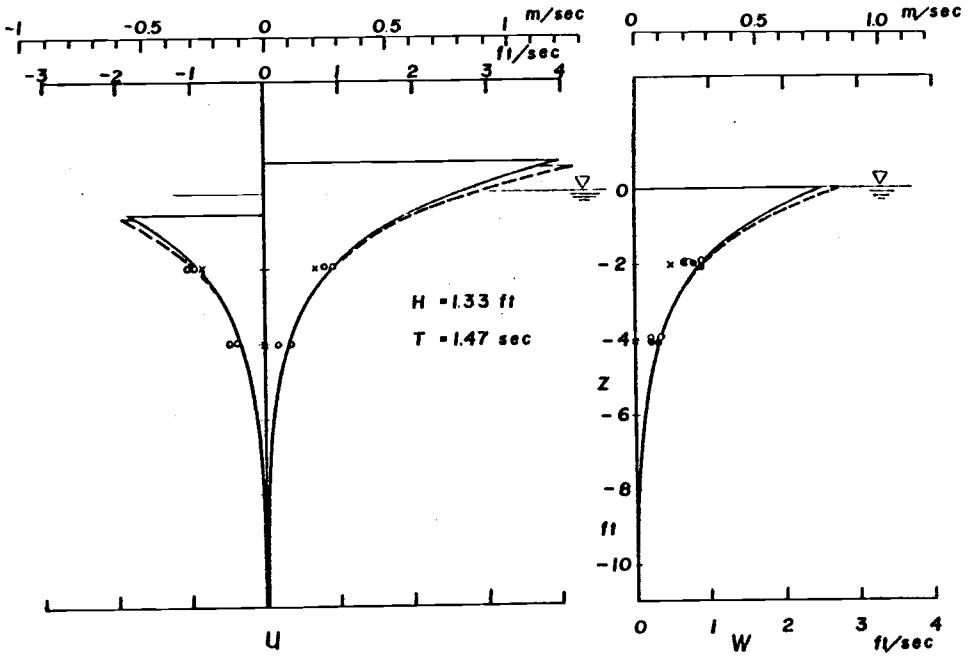

Fig. 4.10 Comparison with theory (5)

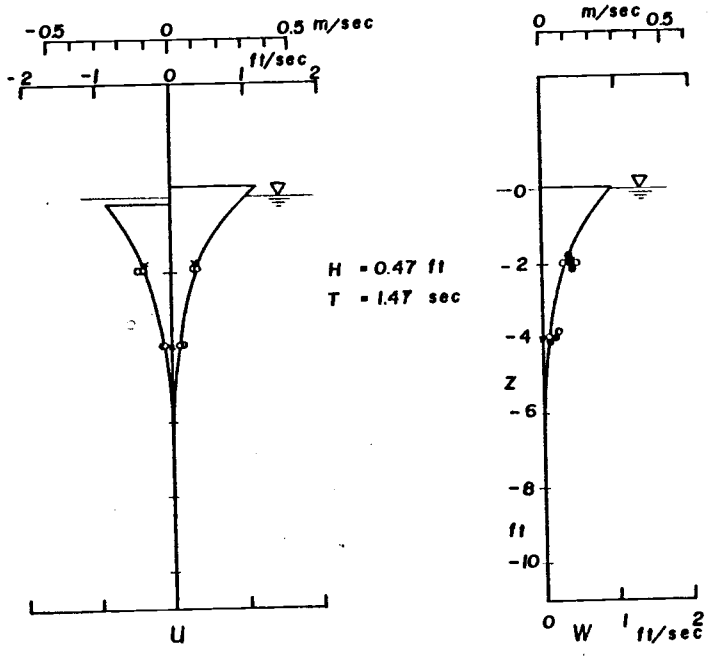

Fig. 4.11 Comparison with theory (6)

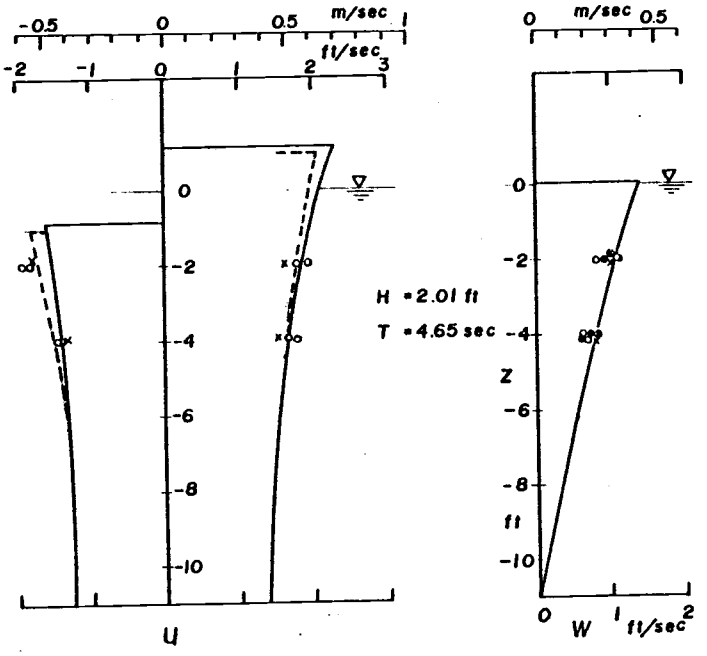

Fig. 4.12 Comparison with theory (7)

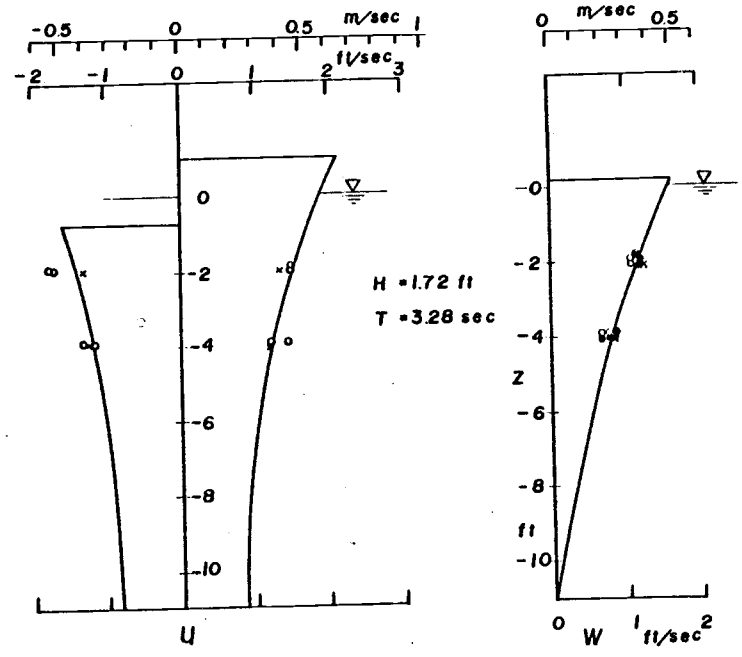

Fig. 4.13 Comparison with theory (8)

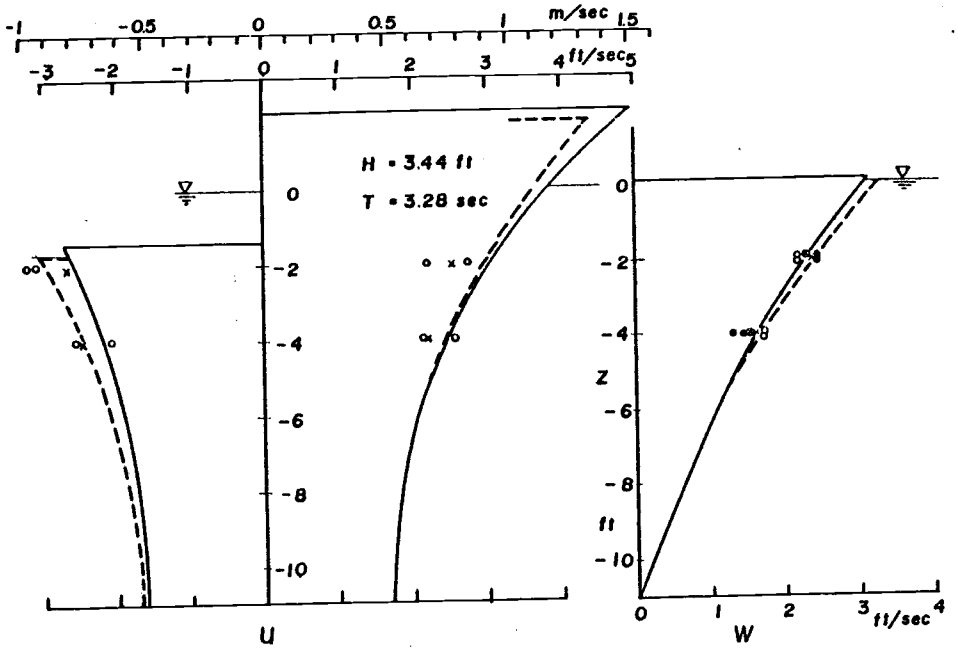

Fig. 4.14 Comparison with theory (9)

Table 4.4 Correlation coefficient of the predicted and measured velocity (periodic wave)

Theory	Level z(ft)	r_c u_+	u_-	w_+	w_-	Mean r_c
Stokes' 5th	-4	0.980	0.988	0.982	0.979	0.984
	-2	0.977	0.986	0.911	0.989	
Airy	-4	0.975	0.983	0.983	0.984	0.982
	-2	0.970	0.981	0.991	0.991	

Table 4.5 Relative error and standard deviation (periodic wave)

Theory	Level z(ft)	u_+	u_-	w_+	w_-
Stokes' 5th	-4	-0.032 (0.201)	0.110 (0.123)	-0.101 (0.211)	-0.071 (0.122)
	-2	-0.043 (0.106)	0.196 (0.089)	0.056 (0.115)	-0.031 (0.111)
Airy	-4	-0.025 (0.209)	0.059 (0.133)	-0.126 (0.213)	-0.098 (0.110)
	-2	-0.040 (0.116)	0.112 (0.120)	0.016 (0.117)	-0.070 (0.095)

Note: The numerals outside and inside the parenthesies represent the mean and standard deviation, respectively.

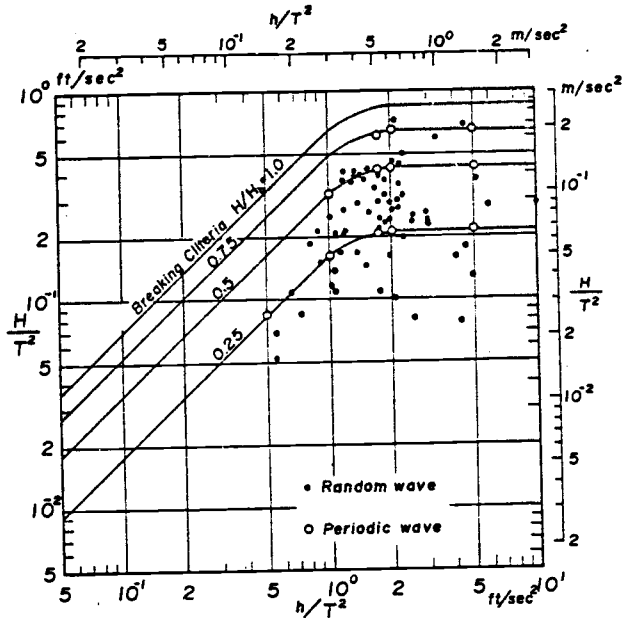

Fig. 4.15 Discrete wave characteristics of random wave (Spectrum I)

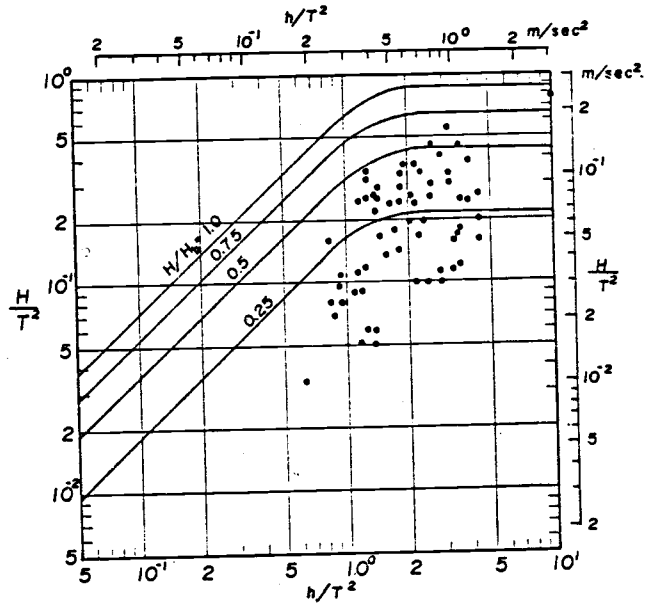

Fig. 4.16 Discrete wave characteristics of random wave (Spectrum II)

Table 4.6 Run designation (random wave)

Series	Run	Position of Hot film	Spectrum	Calibration curve			
				u_+	u_-	w_+	w_-
III	1	-2ft(0.61m)	I	12	11	13	13
	2	-2 (0.61)	II				
	3	-4 (1.22)	I	15	14	16	16
	4	-4 (1.22)	II				

Water depth h = 11 ft (3.35 m)

Calibration curve (Unit: u,w ft/sec, E: volt)

11	u=0.281E	12	u=0.301E
13	w=0.366E	14	u=0.217E
15	u=0.278E	16	w=0.328E

Table 4.7 Parameters of test random waves

Parameter	Spectrum I	Spectrum II
m_0	0.4898	0.3517
m_2	0.07619	0.06179
m_4	0.02078	0.01860
ε^2	0.4300	0.4164
ε	0.656	0.645
$H_{1/3}$ (ft)	2.80(2.77)	2.37(1.98)
$\overline{H}$ (ft)	1.75(1.72)	1.48(1.22)
$T_{1/3}$ (sec)	(2.78)	(2.52)
$\overline{T}$ (sec)	2.54(2.57)	2.39(2.43)

Note: The numerals outside and inside the parentheses represent the value obtained from the measured spectrum and the value obtained from the direct reduction of zero upcrossing wave height and period, respectively.

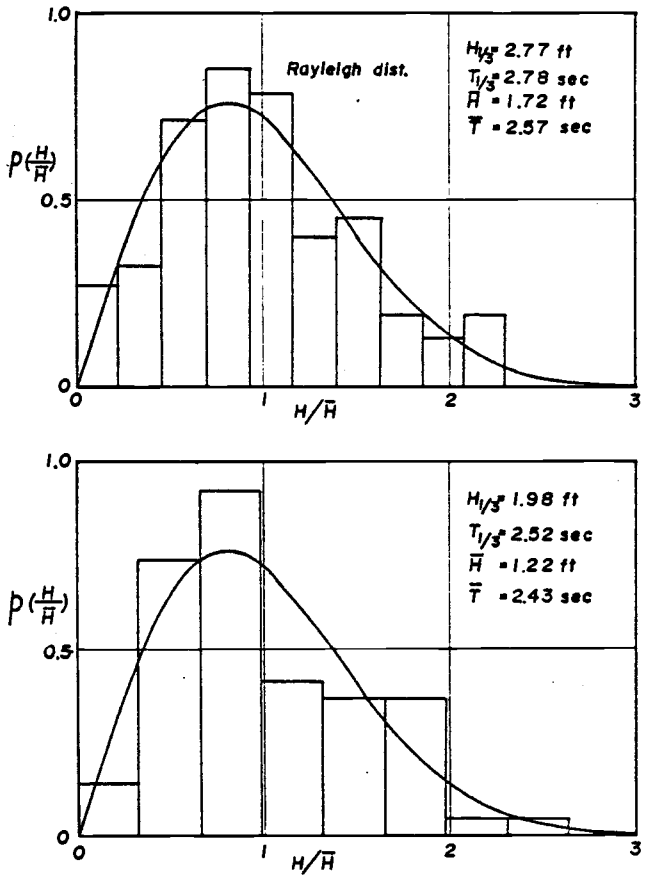

Fig. 4.17 Probability density of wave height

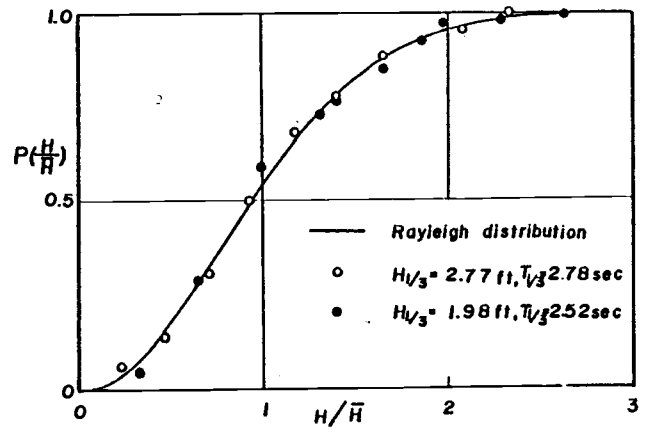

Fig. 4.18 Wave height distribution

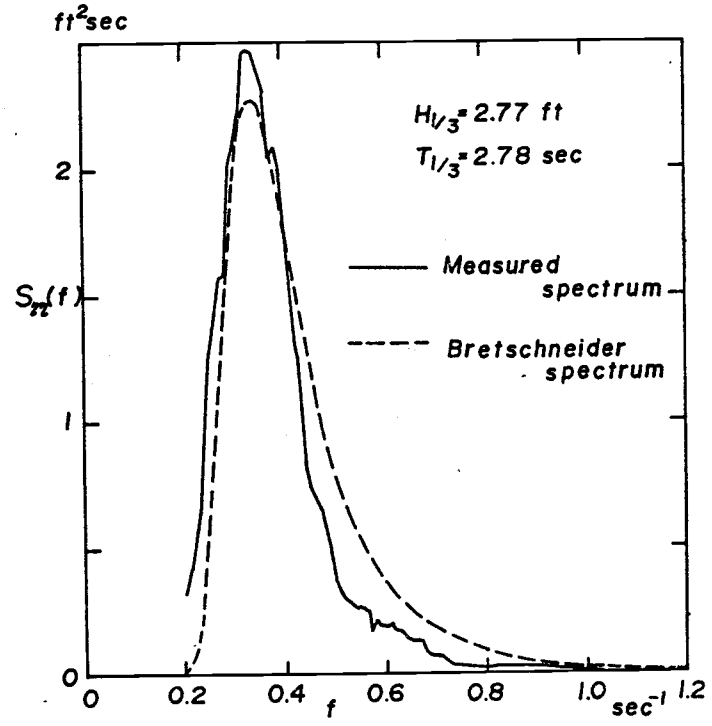

Fig. 4.19 Wave spectrum (Spectrum I)

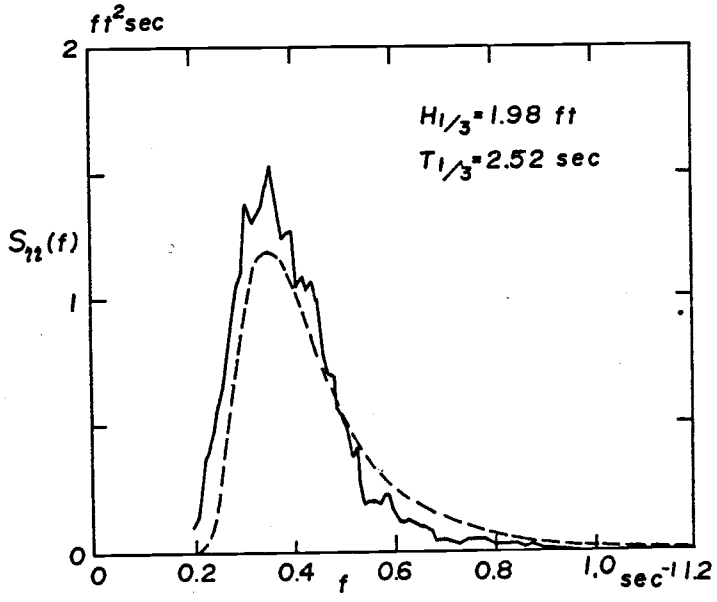

Fig. 4.20 Wave spectrum (Spectrum II)

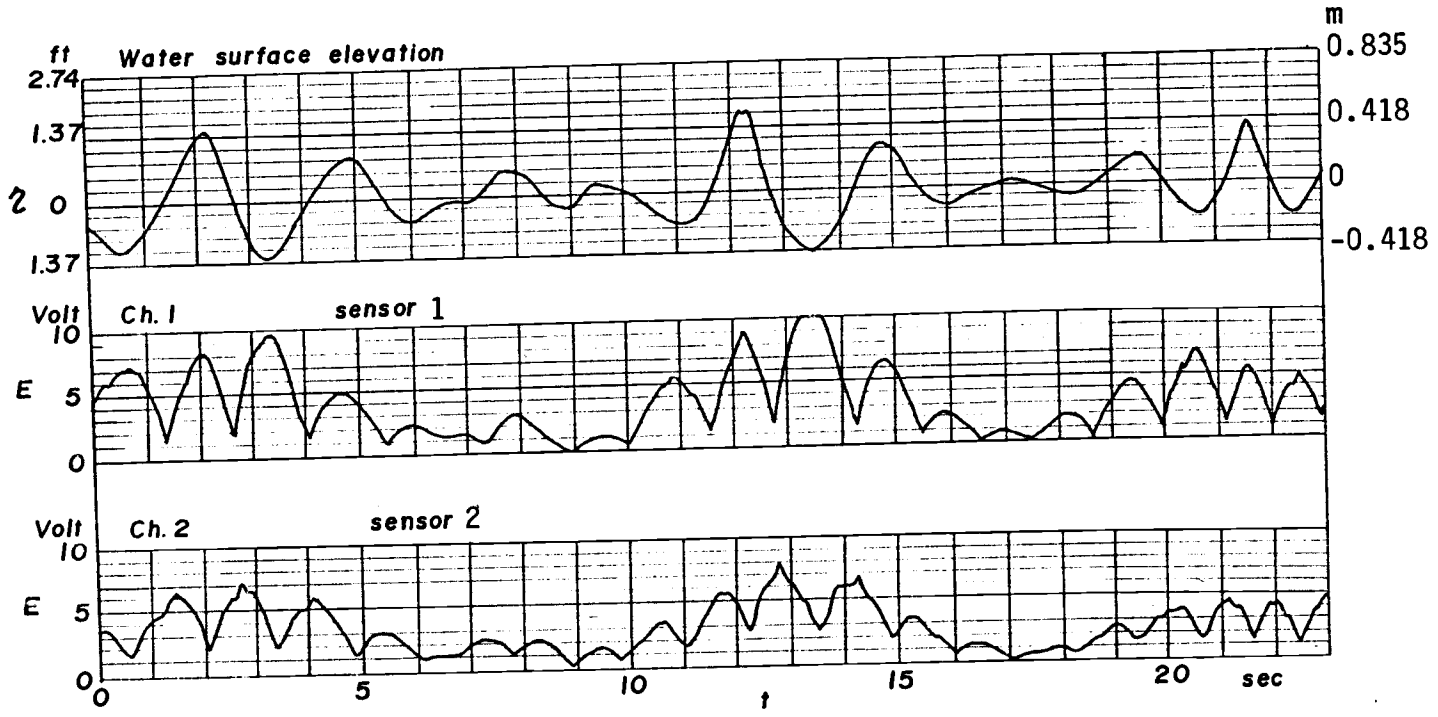

Fig. 4.21 Sample record of random wave test (Spectrum II, z=-2 ft)

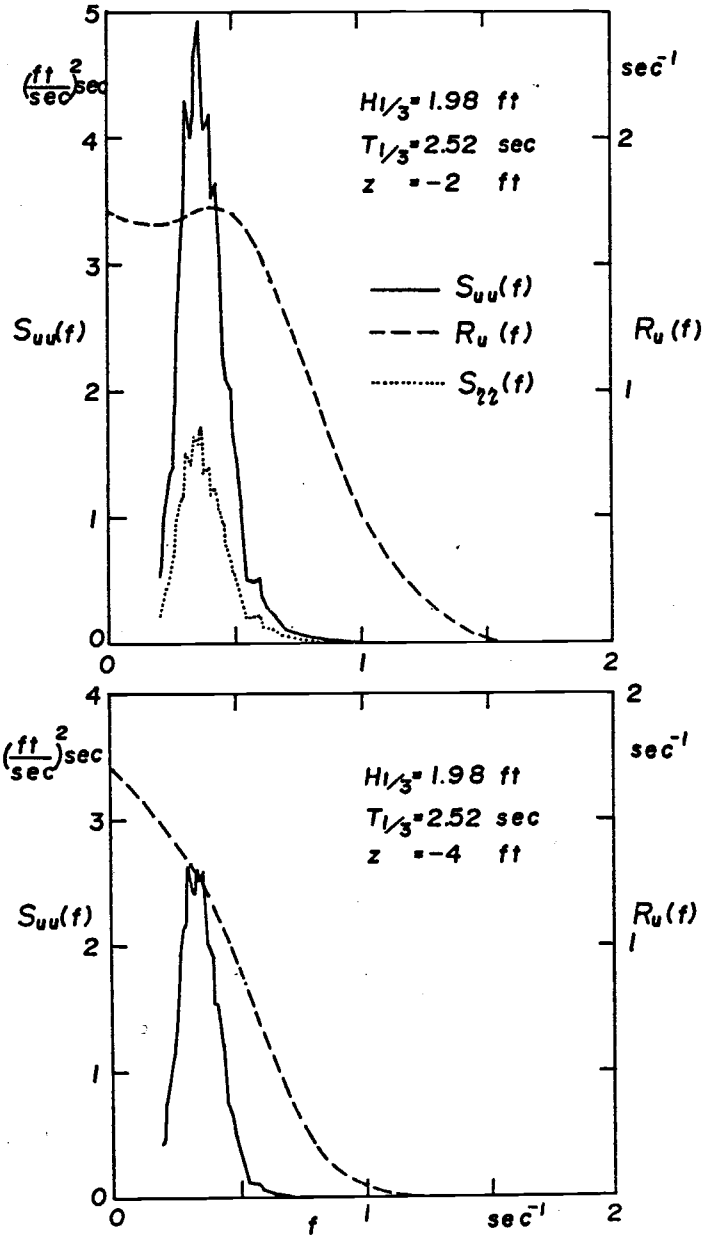

Fig. 5.1 Velocity spectrum (horizontal velocity)

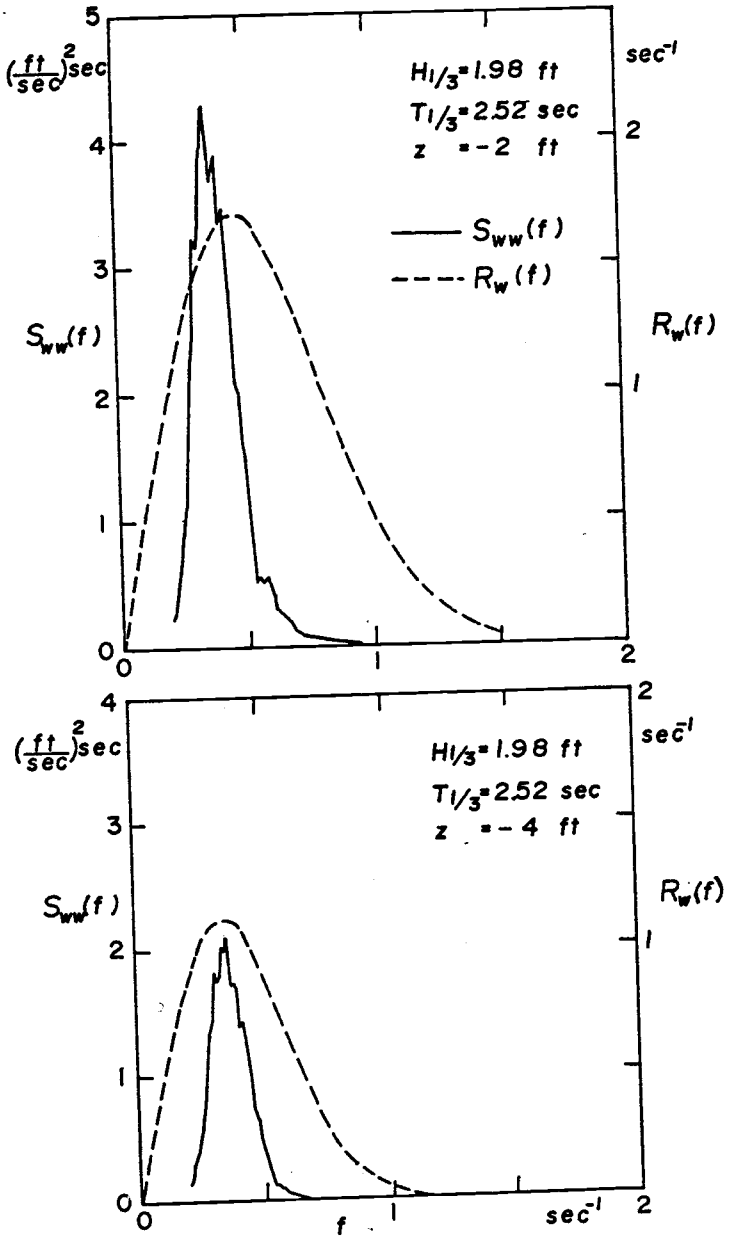

Fig. 5.2 Velocity spectrum (vertical velocity)

Table 5.1 Characteristic values of velocity spectrum (Spectrum I, $H_{1/3}$ =2.77 ft, $T_{1/3}$=2.78 sec)

	u		w		η
	z=-2 ft	z=-4 ft	z=-2 ft	z=-4 ft	
m_0	1.3904	0.7287	1.1369	0.5322	0.4898
m_2	0.1969	0.08729	0.1734	0.01959	0.07619
m_4	0.03750	0.01276	0.0350	0.01095	0.02078
ε	0.507	0.417	0.495	0.411	0.656

Table 5.2 Characteristic values of velocity spectrum (Spectrum II, $H_{1/3}$=1.98 ft, $T_{1/3}$=2.52 sec)

	u		w		η
	z=-2 ft	z=-4 ft	z=-2 ft	z=-4 ft	
m_0	0.9957	0.4872	0.8478	0.3740	0.3517
m_2	0.1572	0.06464	0.1426	0.05378	0.06179
m_4	0.03256	0.01040	0.03091	0.009213	0.01860
ε	0.388	0.419	0.474	0.401	0.645

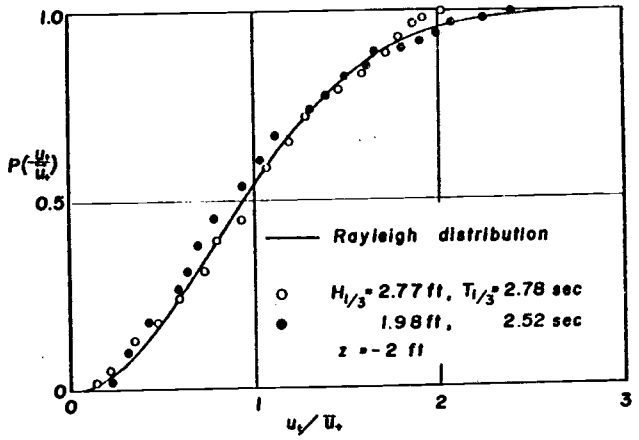

Fig. 5.3 Probability distribution of the velocity beneath wave crests.

Table 5.3 Statistical estimation of velocity

Spectrum	$H_{1/3}$ (ft)	$T_{1/3}$ (sec)	z (ft)	velocity	Experiment $u_{1/10}$	Experiment $u_{1/3}$	Experiment $\bar{u}$	Theory $u_{1/10}$	Theory $u_{1/3}$	Theory $\bar{u}$
I	2.77	2.78	-2	u_+	2.76	2.42	1.51	3.01	2.36	1.47
				u_-	3.02	2.56	1.51	"	"	"
				w_+	2.62	2.33	1.41	2.72	2.13	1.33
				w_-	2.77	2.25	1.32	"	"	"
			-4	u_+	1.98	1.69	1.00	2.18	1.71	1.07
				u_-	2.57	2.16	1.24	"	"	"
				w_+	1.79	1.48	0.89	1.86	1.46	0.91
				w_-	1.64	1.31	0.75	"	"	"
II	1.98	2.52	-2	u_+	2.39	1.86	1.13	2.54	2.00	1.25
				u_-	2.34	1.96	1.18	"	"	"
				w_+	2.35	1.79	1.07	2.35	1.84	1.15
				w_-	1.90	1.52	0.92	"	"	"
			-4	u_+	1.66	1.23	0.72	1.78	1.40	0.87
				u_-	1.92	1.49	0.86	"	"	"
				w_+	1.42	1.04	0.61	1.56	1.22	0.76
				w_-	1.18	0.92	0.53	"	"	"

(Unit: ft/sec)

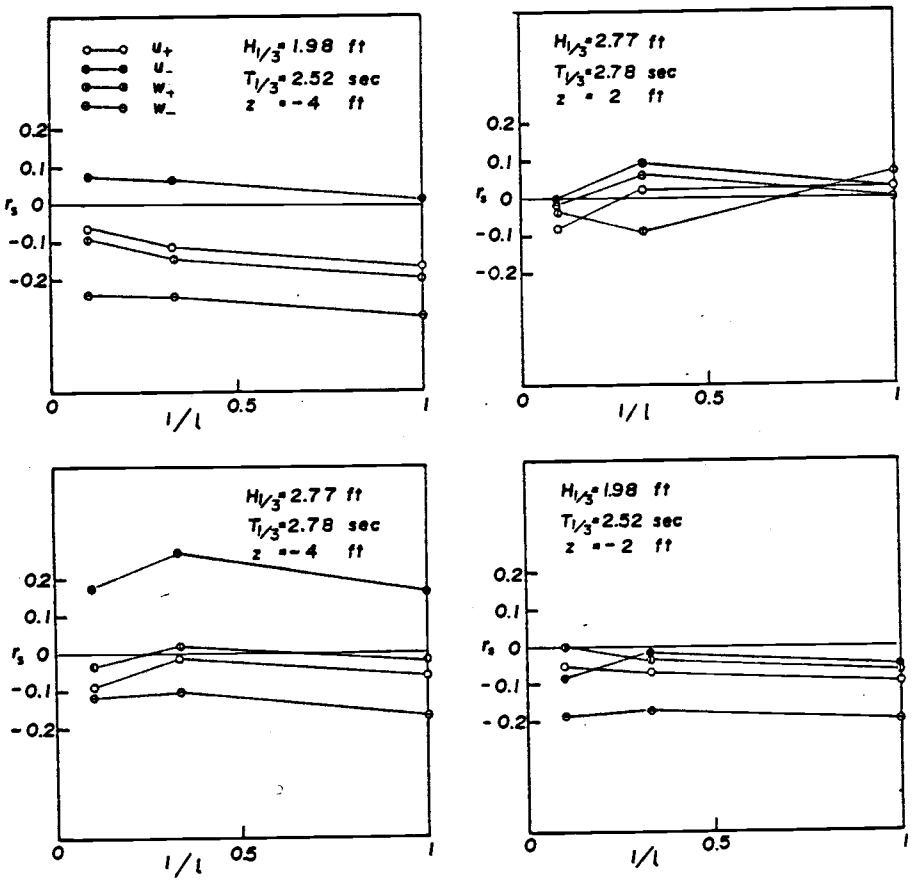

Fig. 5.4 Relative error of statistical estimation

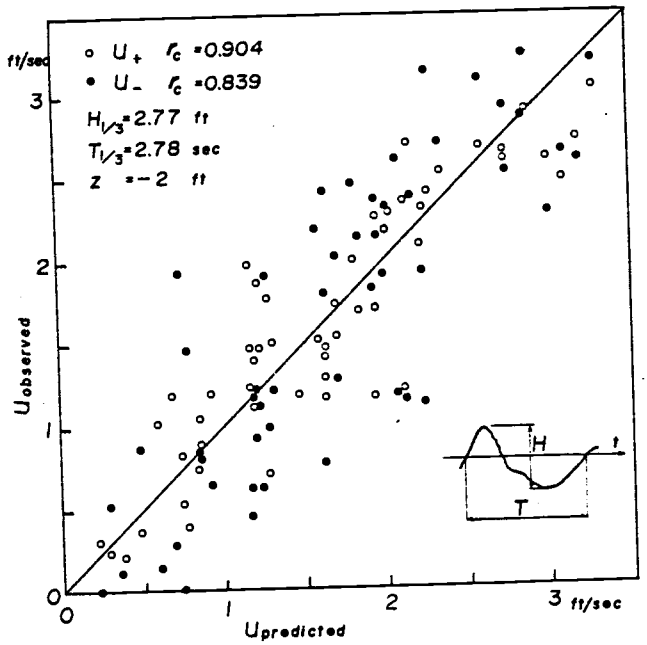

Fig. 5.5 Comparison between predicted and observed velocity (horizontal velocity)

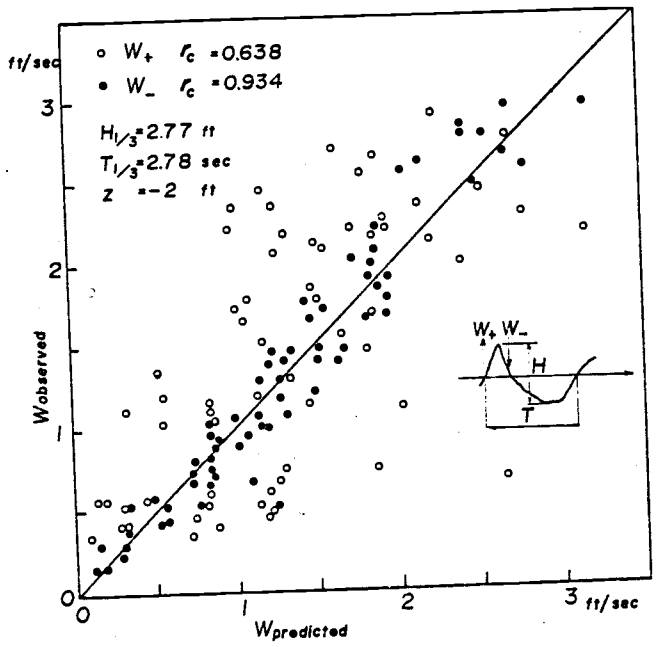

Fig. 5.6 Comparison between predicted and observed velocity (vertical velocity)

Table 5.4 Correlation coefficients and linear regression line (random wave)

Level z(ft)	Velocity	Spectrum I			Spectrum II		
		r_c	a	b	r_c	a	b
-4	u_+	0.803	0.756	0.165	0.873	0.879	0.069
	u_-	0.760	0.939	0.216	0.820	0.980	0.127
	w_+	0.633	0.657	0.309	0.763	0.842	0.066
	w_-	0.956	0.925	0.047	0.889	0.869	-0.009
-2	u_+	0.904	1.003	0.010	0.904	1.039	0.048
	u_-	0.839	1.017	0.054	0.740	1.067	0.019
	w_+	0.638	0.985	0.051	0.606	0.982	0.110
	w_-	0.934	1.005	0.010	0.931	0.922	0.007

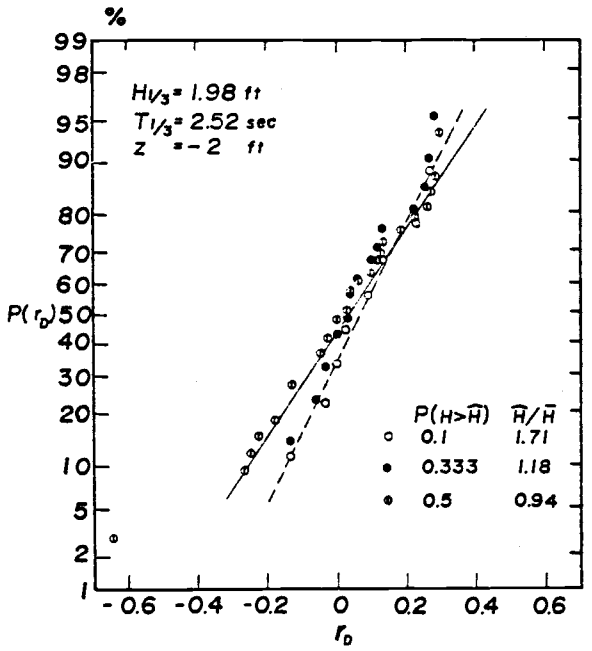

Fig. 5.7 Probability distribution of relative error of u_+

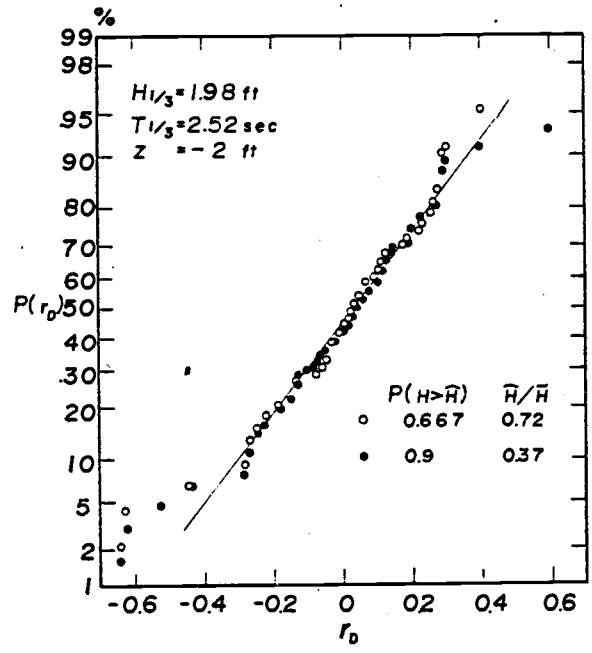

Fig. 5.8 Probability distribution of relative error of u_+

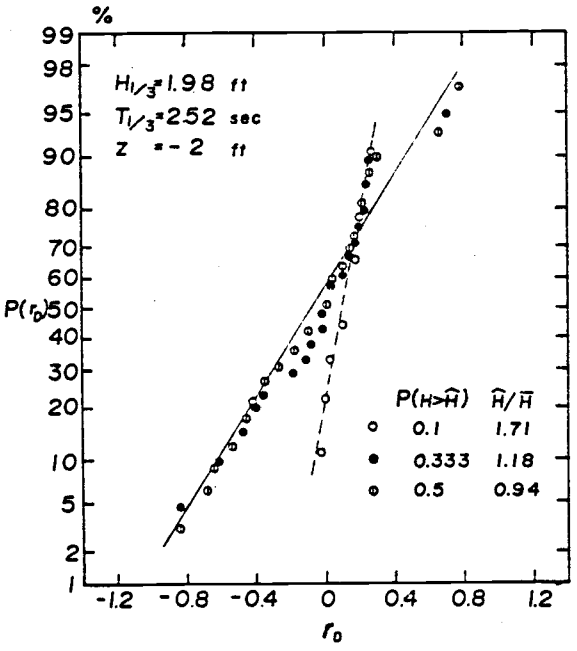

Fig. 5.9 Probability distribution of relative error of W_+

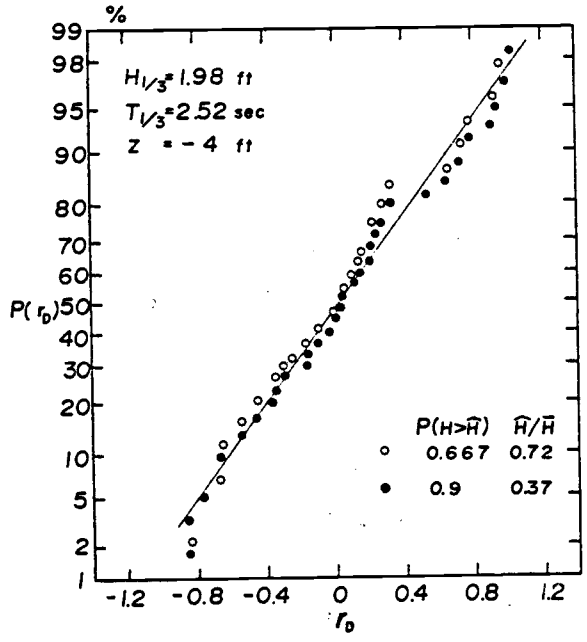

Fig. 5.10 Probability distribution of relative error of W_+

Table 5.5 Chi square test (six degree of freedom)

Spectrum	$H_{1/3}$ (ft)	$T_{1/3}$ (sec)	z (ft)	Velocity	Chi square 1/3	1/2	2/3	9/10
I	2.77	2.78	-2	u_+	3.19	5.76	10.23	8.17
				u_-	3.59	5.40	4.66	8.46
				w_+	2.58	9.86	2.09	5.47
				w_-	8.08	4.00	5.97	5.69
II	1.98	2.52	-2	u_+	7.52	3.76	3.66	10.79
				u_-	2.72	4.57	5.51	8.15
				w_+	8.25	7.84	6.05	9.05
				w_-	10.76	8.67	42.11	60.46
I	2.77	2.78	-4	u_+	9.19	4.50	8.62	8.03
				u_-	5.93	4.51	5.29	7.13
				w_+	4.57	3.21	4.81	5.59
				w_-	4.96	10.40	6.10	8.84
II	1,98	2.52	-4	u_+	4.62	4.24	9.32	11.74
				u_-	8.75	8.29	20.29	28.03
				w_+	5.80	7.20	6.94	9.21
				w_-	11.28	10.89	18.97	49.09

Note: If Chi squre value is larger than 12.59, the fit is not good.

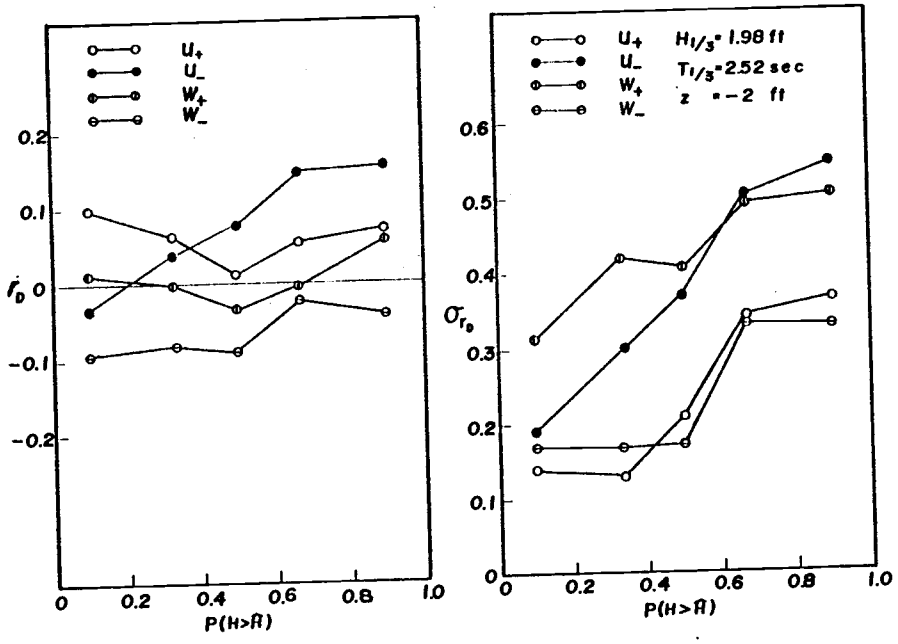

Fig 5.11 Mean and standard deviation of relative error (Spectrum II, z= -2 ft)

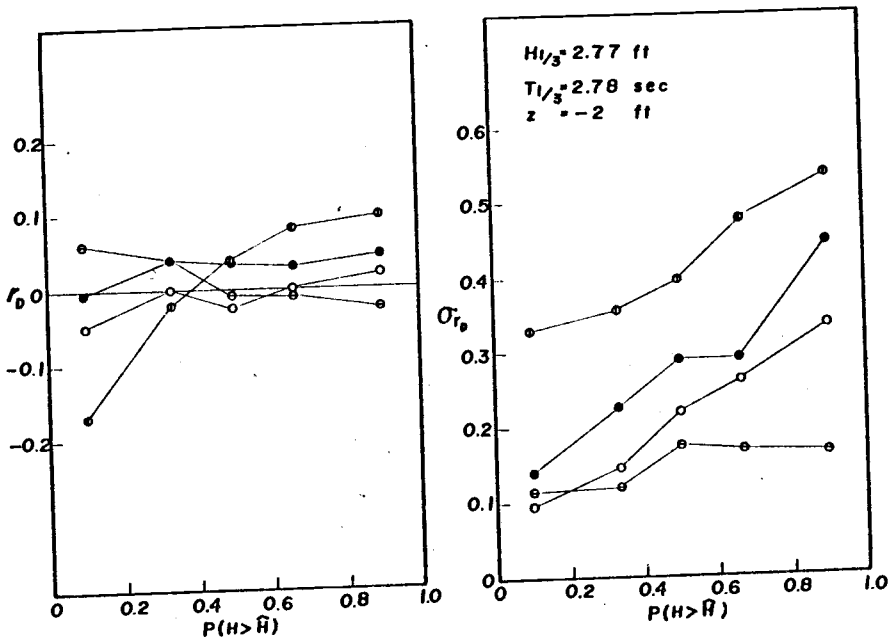

Fig. 5.12 Mean and standard deviation of relative error (Spectrum I, z= -2 ft)

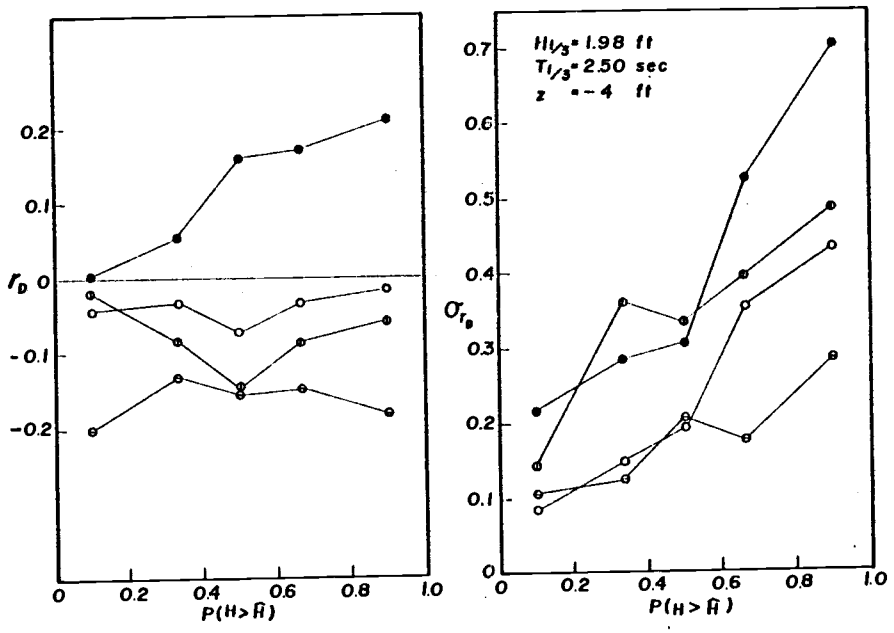

Fig. 5.13 Mean and standard deviation of relative error (Spectrum II, z= -4 ft)

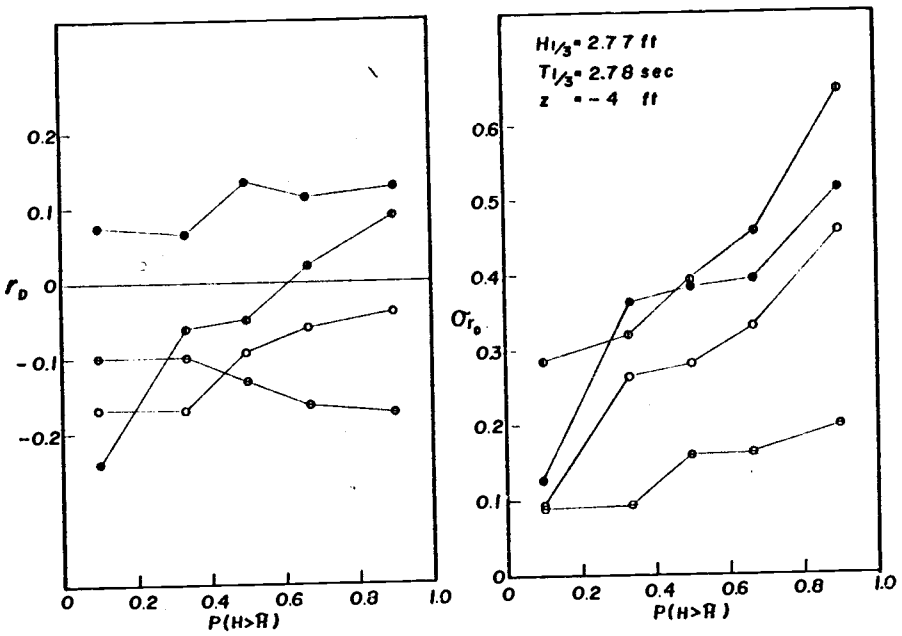

Fig. 5.14 Mean and standard deviation of relative error (Spectrum I , z= -4 ft)

Bibliography

(1) Reid, R.O., Correlation of water level variation with wave forces on a vertival pile for nonperiodic waves, Proc. of 4th Conf. on Coastal Eng., 1958, pp.749-786

(2) Borgman, L.E., Ocean wave simulation for engineering designs, Proc. Conf. on Civil Eng. in the Ocean. A.S.C.E., 1968,pp.31-74

(3) Nath, J.H. and Harleman, D.R.F., Response of vertical cylinder to random waves, Journal of the Waterways and Harbors Division, Proc. of the A.S.C.E., WW2, 1970, pp.373-386

(4) Iwagaki, Y., Sakai, T. and Ishida, H., Correlation of water particle velocity with water level variation for irregular waves, Coastal Eng. in Japan, Vol. 16, 1973, pp.19-28

(5) Reference (1), pp.761

(6) Tsuchiya, Y. and Yamaguchi, M., Horizontal and vertical water particle velocities induced by waves, Proc. of 14th Conf. on Coastal Eng., 1974, pp.555-568

(7) Grace, R.A. and Rocheleau, R.T., Near-bottom velocities under Waikiki swells, James K.K. Look Laboratory of Oceanographic Engineering, Univ. of Hawaii, Technical Report No. 31, 1973, p.55

(8) Grace, R.A., "How to measure waves:, Ocean Industry, Vol. 5, No. 2, 1970, pp.65-69

(9) Goda, Y., Wave forces on a vertical cylinder: Experiments and a proposed method of wave force computation, Report of Port and Harbour Technical Research Institute, Report No. 8, 1964, p.74

(10) Dean, R.G., Evaluation and development of water wave theories for engineering applications, U. S. Army, Corps Engineers Coastal Engineering Research Center, Special Report No. 1, Vol. I, 1974, p.121

(11) LeMehaute, B., Divoky, D. and Lin. A., Shallow water waves: A comparison of theory and experiment, Proc. of 11th Conf. on Coastal Eng., 1968, pp.86-107

(12) Dean, R.G., Relative validity of water wave theories, Proc. A.S.C.E. Specialty Conf. on Civil Eng. in the Oceans, 1968, pp.1-30

(13) Iwagaki, Y. and sakai, T., Horizontal water particle velocity of finite amplitude waves, Proc. 12th Conf. on Coastal Eng., 1970, pp. 309-325

(14) Richardson, E.V. and McQuivey, R.S., Measurement of turbulence in water, Journal of the Hydraulic Division, A.S.C.E., Vol. 94, No. HY2, 1968, pp.411-430

(15) Morrow, T.B. and Kline, S.J., The evaluation and use of hot-wire and hot-film anemometer in liquids, Thermoscience Division, Dept. of Mech. Eng. Stanford Univ., Report MD-25, 1971, p.187

(16) Kato, H. and Sano, K, Characteristics of a hot-film anemometer for the measurement of turbulence in water, Technical Note of the Port and Harbour Research Institute, No. 157, 1973, p.21

(17) Skjelbreia, L., Gravity waves, Stokes' third order approximation, Table of function, Council on Wave Research, The Engineering Foundation, 1959, pp.1-337

(18) Iwagaki, Y., Hyperbolic waves and their shoaling, Proc. 11th Conf. on Coastal Eng., 1968, pp.124-144

(19) Kolpak, M.M. and Eaglson, P.S., A system for measuring orbital velocities in waves, Proc. 12th Conf. on Coastal Eng., 1970, pp.327 -343

(20) Van Dorn, W.G. and Pazan, S.E., Laboratory investigation of wave breaking, Part II: Deep water waves, Advanced Ocean Eng. Laboratory Report No. 71, Scripps Instituttion of Oceanography, Univ. of California, Sandiego, 1975, p.105

(21) Lee, A., Grated, C.A. and Durrani, T.S., Velocities under periodic and random waves, Proc. of 14th Conf. on Coastal Eng., 1974, pp.558 -574

(22) Sollit, C.K. and Hurber, D.S., Large scale model testing of a submerged wave attemuation device, Closed Loop, MTS System Corporation, 1976, pp.13-26

(23) Reference (20), pp.84-88

(24) Dean, R.G., Evaluation and development of water wave theories for engineering application, Special Report No. 1, U.S. Army, Corps of Engineers, Coastal Engineering Research Center, Vol. II, 1974, p.534

(25) Skjelbreia, L. and Hendrickson, J., Fifth order gravity wave theory, Proc. of 7th Conf. on Coastal Eng., 1960, pp.184-196

(26) Ippen, A.T., Estuary and coastline hydrodynamics, McGraw-Hill Book Co., Inc., 1966, pp.28

(27) Bendat, J.S. and Piersol, A.G., Random data: Analysis and measurement procedure, Wiley-interscience a Division of John Wiley and Sons, Inc., 1971, pp.325-326

(28) Cartwright, D.E. and Longuet-Higgins, M.S., The statistical distribution of maxima of a random function, Proc. of Royal Society A237 (1209), 1956, pp.212-232

(29) Kinsman, B., Wind Waves, Prentice-Hall, Inc., 1965, pp.134

(30) Hinza, J.O., Turbulence, McGraw-hill Book Company, 1959,pp.103

(31) Reference (27), pp.136-137

(32) Meyer, S.L., ta analysis for scientists and engineers, John Wiley and Sons, Inc., 1975, pp.355-358

(33) Reference (26), pp.156

APENDICES

Appedix I List of symbols

a : coefficient in the linear regression relation, Eq.(5.14)

a_m : coefficients in Reid's numerical filter, Eq. (2.1)

$A(f)$: Fourier cosine transform of $\eta(t)$, Eq. (4.8)

$A(\theta)$: directional coefficient, Eq. (3.2)

b : coefficient in the linear regression relation, Eq. (5.14)

b_m : coefficients in Reid's numerical filter, Eq.(2.2)

$B(f)$: Fourier sine transform of $\eta(t)$, Eq. (4.9)

C_i : coefficients of approximating polynomial of the linearizer, Eq. (3.1)

E : linearized output voltage from the hot film anemometer

E_B : non-linear output voltage of the hot film anemometer

E_0 : non-linear output voltage at zero flow

E_{1min} : minimum linearized output voltage (Ch.1, vertical sensor)

E_{2min} : minimum linearized output voltage (Ch.2, horizontal sensor)

E_{1max} : maximum linearized output voltage (Ch.1, vertical sensor)

E_{2max} : maximum linearized output voltage (Ch.2, horizontal sensor)

f : wave frequency (sec^{-1})

$\tilde{G}_x(f)$:raw estimate of power spectral density

$G_x(f)$: smooth estimate of power spectral density

h : water depth

$\overline{H}$: wave height

$\overline{H^2}$: mean squar of zero upcrossing wave height

$\overline{H}$: mean zero upcrossing wave height

$H_{1/3}$: significant wave height

H_D : design wave height

H_p : measured wavw height with pressure gauge

i : index

j $= \sqrt{-1}$

k : wave number ($k=2\pi/L$)

K : coefficient in Eq. (4.2)

L : wave length

L_A : wave length given by Airu theory

m : index

m_ν : νth moment of a spectrum about the origin

N : number of the record

n : frequency of the output pulses from the propeller current meter (coefficient in Eqs. (2.15) and (2.16) in Chapter 2)

$p(x)$: probability density

$P(x)$: cumulative probability

$R_u(\omega)$: frequency response function for horizontal velocity

$R_w(\omega)$: frequency response function for vertical velocity, Eq. (2.6)

$R'_u(f)$: frequency response function for horizontal velocity, Eq. (5.4)

$R'_w(f)$: frequency response function for vertical velocity, Eq. (5.4)

r_c : correlation coefficient

r_D : relative error of velocity estimate with periodic wave theory

$\overline{r}_D$: mean of r_D

r_p : relative error of velocity estimate for periodic waves

r_s : relative error of statistical velocity estimate

$S_{\eta\eta}(f)$: spectral density of water surface elevation

$S_H2(\omega)$: Bretschneider spectrum

$S_{uu}(f)$: spectral density of horizontal velocity fluctuation

$S_{ww}(f)$: spectral density of vertical velocity fluctuation

T : wave period

$T_{1/3}$: significant wave period

$\overline{T}$: mean zero upcrossing wave perios

T_D : design wave period

t : time

t_1, t_2: the times when a record starts and ends, respectively

u : horizontal velocity

u_+ : horizontal velocity beneath wave crests

u_- : horizontal velocity beneath wave troughs

u_n : normal velocity component to the hot film axis, Eq. (4.2)

u_t : tangential velocity component to the hot film axis, Eq. (4.2)

V : magnitude of flow speed

v_{max} : maximum speed of the pendulum motion

w : vertical velocity

w_+ : vertical velocity when the water surface crosses the still water level upward

w_- : vertical velocity when the water surface crosses the still water level downward

$X(f)$: Fourier transform of water surface elevation, $\eta(t)$

z : vertical distance from the still water level (upward positive)

$\alpha(\theta)$: directional coefficient, Eqs. (2.15) and (2.16)

θ : yaw angle, the angle between flow direction and hot film sensor axis

τ : time interval

$\eta(t)$: water surface elevation

$\overline{\eta^2}$: mean square of water surface elevation

σ_{r_D} : stadard deviation of r_D

Appendix II Calibration of the propeller current meter and the hot film anemometer

A.1 Calibration aparatus

The calibration of the propeller current meter and the hot film anemometer have been usually conducted in a steady flow utilizing a water tunnel, water jet or moving carriage. However, since alternating flows due to a wave motion is of interest for the present measurement, it is desirable that the calibrations be conducted in an oscillatory flow. Thus, a pendulum which could generate a damped oscillation and a carriage which was manually swayed to and fro were used.

The range of the periods of the pendulum and the carriage motion were from two seconds to three seconds. The significant wave periods of the test random waves fall into this range.

(1) Pendulum (Fig. A.1)

The rod is composed of aluminum tubes and iron channels. It is stiff enough so that the transverse vibration due to the Karman vortex trail is small. The displacement of the pendulum was measured utilizing the Sonic Wave Profiler. Figure A.2 shows the sketch of a typical record of the free damped oscillation of the pendulum.

The maximum speed at the end of the pendulum, which is used to obtain the relation of the outputs from the propeller current meter or hot film anemometer to the flow speed, is calculated as follows.

A free damped oscillation of a linear system is expressed as

$$x = a_0 \exp(-\zeta\omega_0 t) \cos(\sqrt{1-\zeta^2}\,\omega_0 t) \qquad (A.1)$$

where x is the displacement of the end of the pendulum, a_0 is the initial displacement, ζ is a damping coefficient (linear saaumption), ω_0 is the undamped natural frequency of the pendulum and t is a time.

From the record, ζ and ω_n are calculated with the following equations.

$$\sqrt{1 - \zeta^2}\,\omega_0 = 2\pi / \overline{T} \qquad (A.2)$$

where $\overline{T} = \frac{1}{N} \sum_{i=1}^{N} T_i$.

$$\exp(-\zeta\omega_0\overline{T}) = \overline{a_{i+2}/a_i} \qquad (A.3)$$

where $$\overline{a_{i+2}/a_i} = \frac{\sum_{i=0}^{N-1} [(a_{2i+2}/a_{2i}) + (a_{2i+3}/a_{2i+1})]}{2(N - 1)}$$

When the damping coefficient ζ is much smaller than 1.0, above equation can be written as

$$\omega_0 = 2\pi / \overline{T} , \qquad (A.4)$$

$$\exp(-2\pi\zeta) = \overline{a_{i+2}/a_i} . \qquad (A.5)$$

Now , the velocity of the pendulum, v, is obtained by differenciating Eq. (A.1) with respect to time, t.

$$v = a_0\omega_0 \exp(-\zeta\omega_0 t) \sin (\sqrt{1 - \zeta^2}\,\omega_0 t - \phi) \qquad (A.6)$$

where $$\phi = \mathrm{Tan}^{-1} \frac{\zeta}{\sqrt{1 - \zeta^2}}$$

When the damping coefficient ζ is small, ϕ is very small. For small damping coefficient, Eq. (A.6) gives the amplitudes of the velocity as

follows.

$$(v_{max}) = a_0 \omega_0 \exp\{ -\zeta \omega_0 (i+\tfrac{1}{2})T/2 \} \qquad (A.7)$$

$$= a_0 \omega_0 \exp\{-\zeta\omega_0 iT/2\} \exp(-\zeta\omega_0 T/4)$$

$$i = 0,1,2,.....,N$$

On the other hand, the amplitude of the displacement is obtained from Eq. (A.1) as

$$a_i = a_0 \exp\{-\zeta\omega_0 iT/2\}, \qquad (A.8)$$

$$a_{i+1} = a_0 \exp\{-\zeta\omega_0 (i+1)t/2\}$$

$$= a_0 \exp\{-\zeta\omega_0 iT/2\} \exp(-\zeta\omega_0 T/2) \quad . \qquad (A.9)$$

The function exp(-y) is expressed in the Taylor expansion.

$$\exp(-y) = 1 - y + \frac{1}{2} y^2 - \frac{1}{6} y^3 + ... \qquad (A.10)$$

Hence, for small damping coefficient ζ, Eq. (A.7) and Eq. (A.9) can be approximated as follows.

$$(v_{max})_i = a_0\omega_0 \exp\{-\zeta\omega_0 iT/2\} (1 - \zeta\omega_0 T/4) \qquad (A.11)$$

$$a_{i+1} = a_0 \exp\{-\zeta\omega_0 iT/2\} (1 - \zeta\omega_0 T/2) \qquad (A.12)$$

From Eq. (A.8), (A.11) and (A.12), the maximum velocity is expressed in terms of the amplitudes of the pendulum displacement.

$$(v_{max})_i = \omega_0 \frac{a_i + a_{i+1}}{2}, \qquad \text{at } t = (i + \tfrac{1}{2}) \tfrac{T}{2} \qquad (A.13)$$

Thus the maximum velocities are theoretically calculated from the displacement records. They are compared with the output from the propeller

current meter and the hot film anemometer.

(2) Carriage (Fig. A.3)

A T-shaped carriage was also used to calibrate the propeller current meter. Since the carriage was manually driven, the motion was no longer sinusoidal. So, the speed of the carriage was calculated as the slope of the displacement record which was measured with a pair of the Sonic Wave Profilers.

$$v = \frac{\Delta x}{\Delta t} \tag{A.14}$$

where Δt is a time interval and Δx is the displacement of the carriage in the time interval Δt.

The above calculated speed was compared with the output from the propeller current meter in the calibration.

A.2 Calibration

(1) Propeller current meter

As mentioned in Chapter 3, the output from the propeller current meter is the pulses which are generated by the passage of the blades past the gold tip within the head of the support. Figure A.4 shows the relation of the maximum frequencies of the pulses to the maximum speeds calculated from Eq. (A.13), during one trial of the damped oscillation of the pendulum. The relation is well approximated by a straight line, Eq. (A. 15).

$$n = 4.39\ v_{max} - 4.45 \tag{A.15}$$

where n is the frequency of the output pulses (Hz), i.e. $n=1/\Delta t$, Δt is the time interval between two adjacent pulses and v_{max} is the maximum

speed of the pendulum (inch/ sec). The line given by above equation fits the frequency-maximum speed correlation in high speed range (Fig. A.5) which was tested utilizing the T-shape carriage.

Having obtained the relation of the pulse frequency to the flow speed, one can reduce the output pulses to flow speed at any stage during one cycle of the pendulum oscillation. The measured time variation of the flow speed is compared with the theoretical variation, Eq. (A. 16) in Fig. A.6.

$$\frac{v}{v_{max}} = \frac{\exp(-\zeta \omega_0 t) \sin(\sqrt{1-\zeta^2}\,\omega_0 t)}{\exp(-\zeta \omega_0 T/4)}, \quad 0 < t < T \qquad (A.16)$$

Though the observed variation is not smooth due to the accuracy of record reading, it agrees quite well with the theoretical variation. Some differences of the measured speed from the theoretical variation are seen in the low speed range. This is because the relation, Eq. (A.15), can not hold such a range. Thus it can be said that the propeller has good response to oscillating flow within the frequencies tested.

The flow in waves changes its magnitude and direction, and it is generally expressed by the horizontal and vertical components. It is thus desirable that the propeller responds only to the velocity component which direction is parallel to the propeller spindle. The angular response was tested utilizing the pendulum and twisting the propeller probe by θ = 30, 45 and 60 degrees. The angle was measured with the scale marked on the aluminum tube (see Fig. A.1), so the ambiguity of the angle was $\pm$ 5 degrees.

The results are plotted in Fig. A.7. The relation between the maximum frequency of the pulses and the flow speed for each propeller angle can be

expressed by a straight line. The slpoe the the line decreases according to the increase of the angle, θ. The change of the propeller response due to the angle is clearly shown in Fig. A.8. The dots in the figure show the relation given by the straight lines for respective angles in Fig. A.7, and they agree with the curve given by Eq. (A.17).

$$n = 4.39\ v_{max}\cos\ \theta - 4.45 \qquad (A.17)$$

(2) Hot film anemometer

All the calibrations of the hot film anemometer were conducted utilizing the pendulum. A typical record of the linearized output from sensor 1 (outer sensor) is shown in Fig. A.9, and that of sensor 2 (inner sensor is shown in Fig. A.10. In these figures, theoretical curve of the damped free oscillation given by Eq. (A.18) is plotted with dotted line.

$$E = E_{max,0}\ \exp(-\zeta\omega_0 t)\ \sin(\sqrt{1-\zeta^2}\,\omega_0 t) \,/\, \exp(-\zeta\omega_0 T/4) \qquad (A.18)$$

where $E_{max,0}$ is defined as shown in the figures, ζ and ω_0 are calcurated from Eq. (A.4) and Eq. (A.5) respectively. For this case, the damping coefficients ζ is 0.0133 and ω_0 is 2.161 radian per second. very other peak of the linearized output from the outer sensor is smaller than that of the theoretical curve (Fig. A.9). On the other hand variation of the output from the inner sensor is very close to the theoretical one (Fig. A.10). This shows the the response characteristics of the outer sensor to the flow of one direction is different from that to the flow of opposite direction.

Taking such characteristics of the outer sensor into account, it can be said that the agreement of these two curves is fairly good and that the

linearizers functioned well.

It is well known that the relation between fluid speed and output voltage from a hot film anemometer is easily affected by dirt and fluid temperature change. Therefore, the hot film anemometer was calibrated at the begining and the end of each series of runs. The first half runs were processed using the result of the calibration at the begining while the latter half runs were processed using that at the end.

Fig. A.11 through A.14 show the relations of the maximum output voltage to the maximum speed, Eq. (A.13) obtained from the calibrations. The slope of the calibration curve decrease after a series of runs due to the dirt and the temperature change. The relations given the these curves are listed in Table 4.1 and Table 4.7 (Chapeter 4).

The angular sensitivity of each sensor was examined in the same way as the propeller probe was tested. Figures A.15 and A.16 show the results for the outer sensor (Ch. 1) and the inner sensor (Ch. 2) respectively. The difference between the angular sensitivity of these two sensor is obvious: the outer sensor is very sensitive to the angle θ while the inner sensor shows same E-v relation over the range $\theta \leqslant 60$ degree.* Thus the angular sensitivity of a hot film sensor varies from sensor to sensor.

---

* The test for another probe yielded opposite result: the outer sensor did not have any angular sensitivity over the range $\theta \leqslant 45^{\circ}$ while the inner sensor showed remarkable angular sensitivity as Fig. A.15.

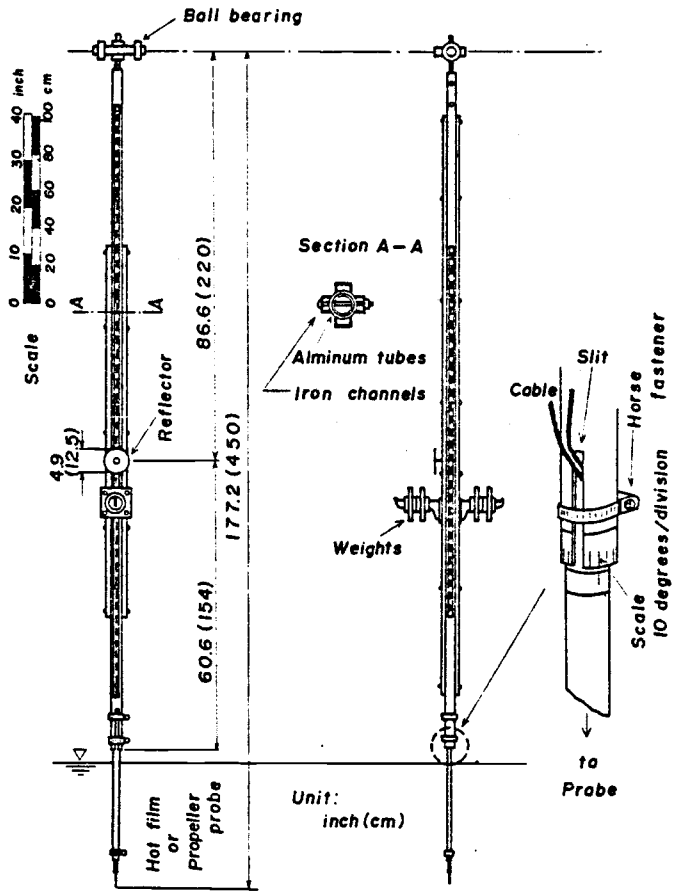

Fig. A.1 Pendulum

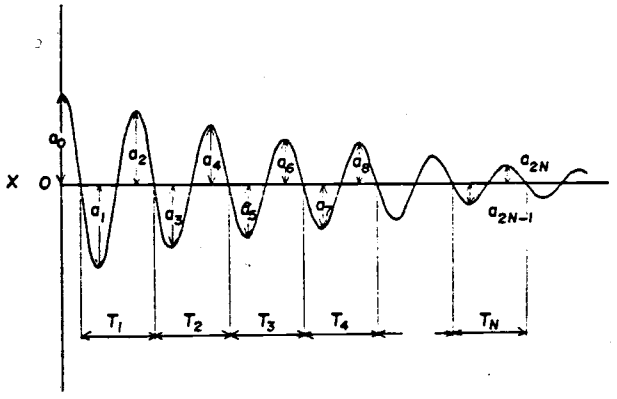

Fig. A.2 Sketch of a record of pendulum motion

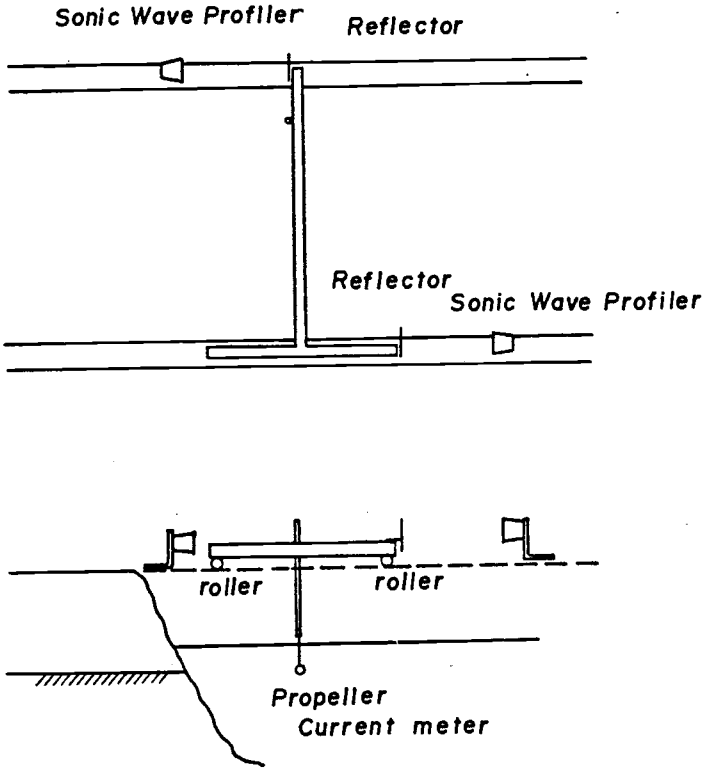

Fig. A.3 T-shape carriage

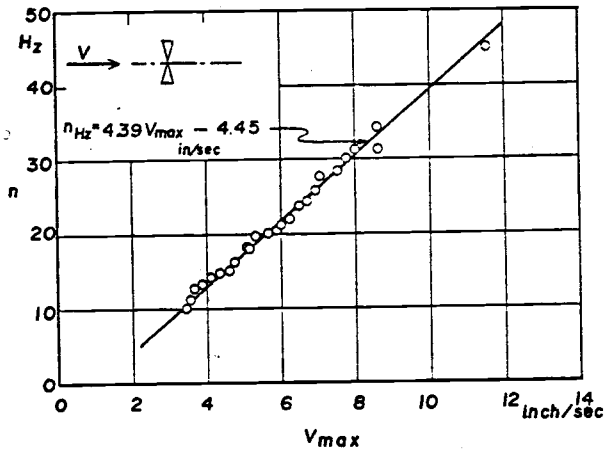

Fig. A.4 Calibration of propeller current meter for low speed range

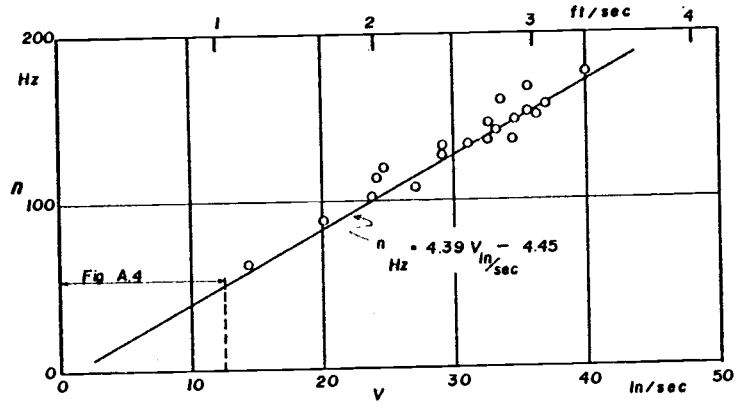

Fig. A.5 Calibration of propeller current meter for high speed rangr with T-shape carriage

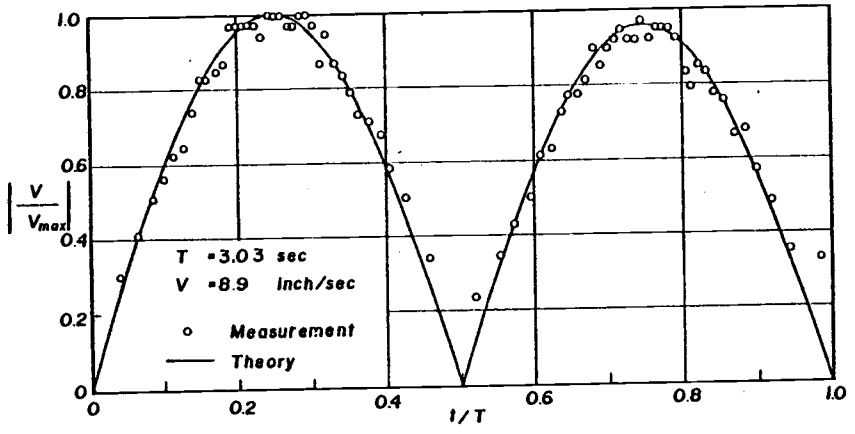

Fig. A.6 Response of propeller

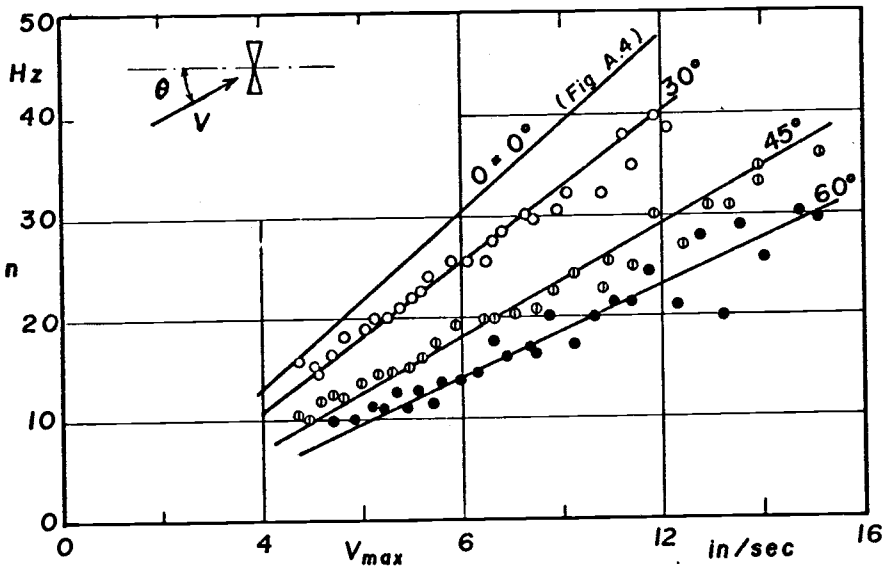

Fig. A.7 Effect of flow direction on propeller response

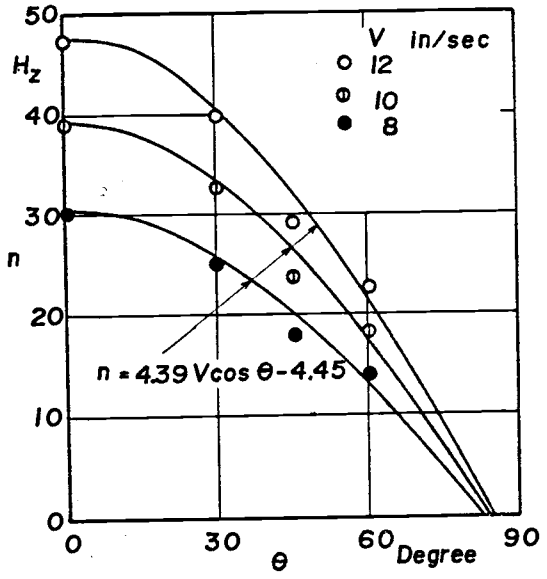

Fig. A.8 Angular sensitivity of propeller

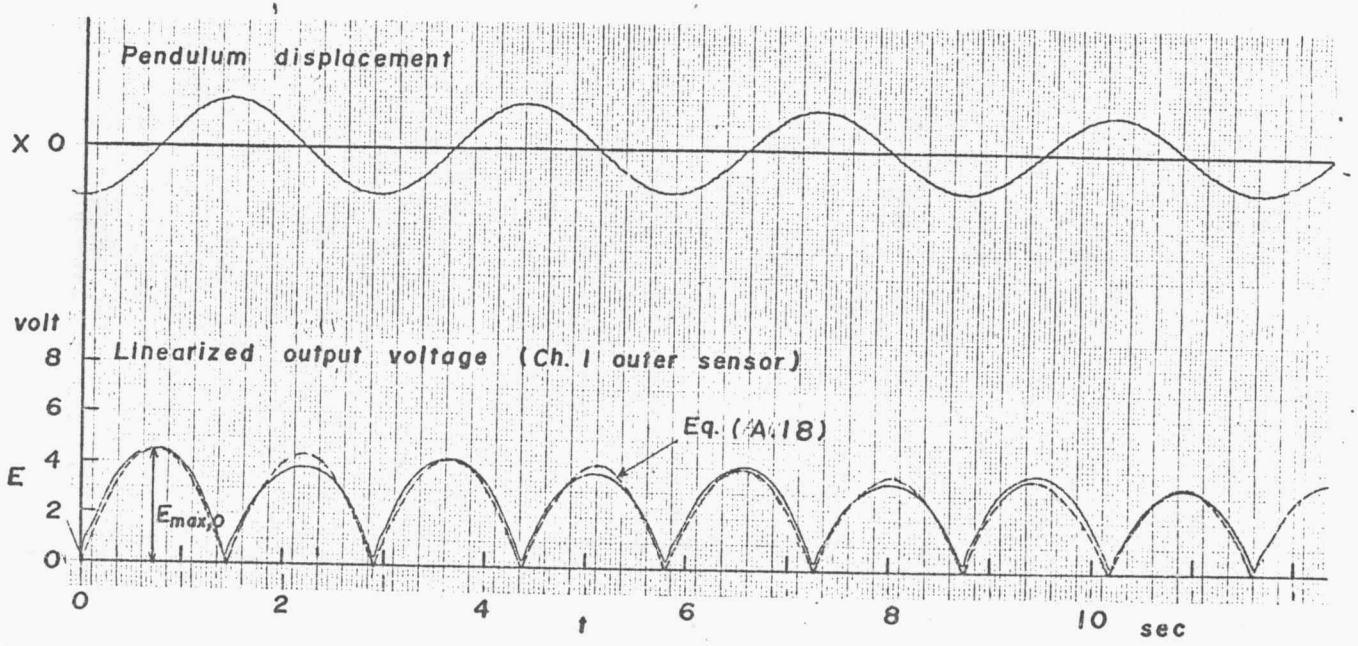

Fig. A.9 Response of hot film anemometer to an oscillatory flow (vertical sensor)

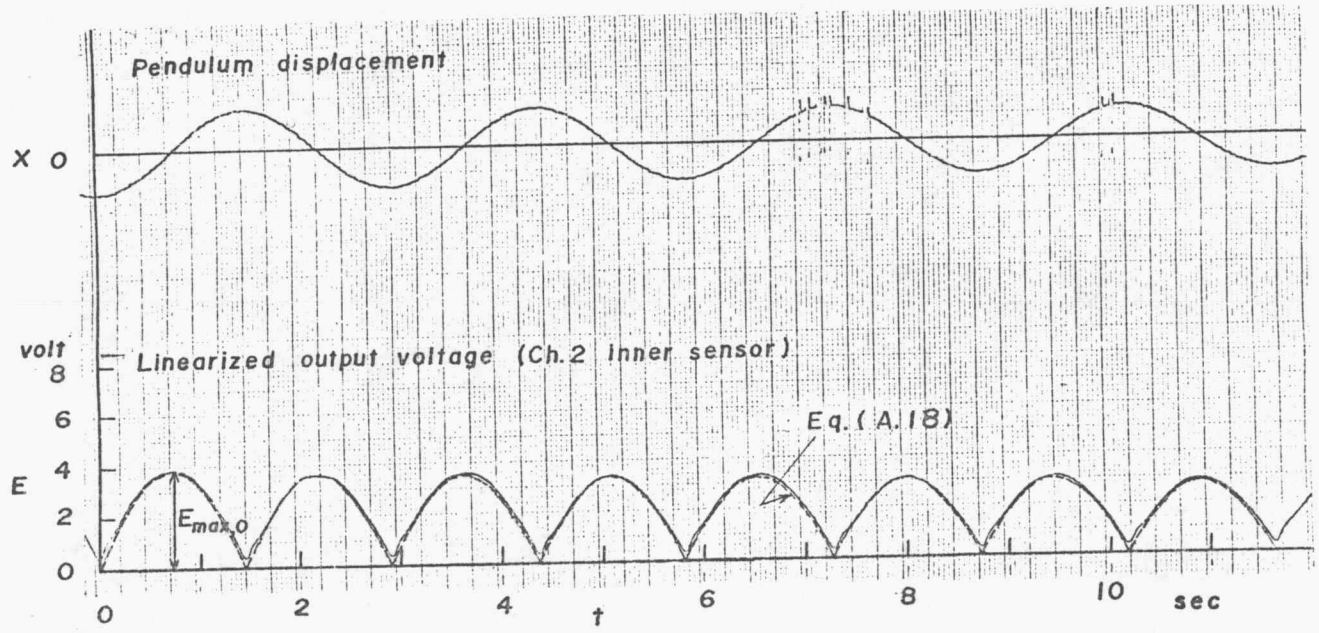

Fig. A. 10 Response of hot film anemometer to an oscillatory flow (horizontal sensor)

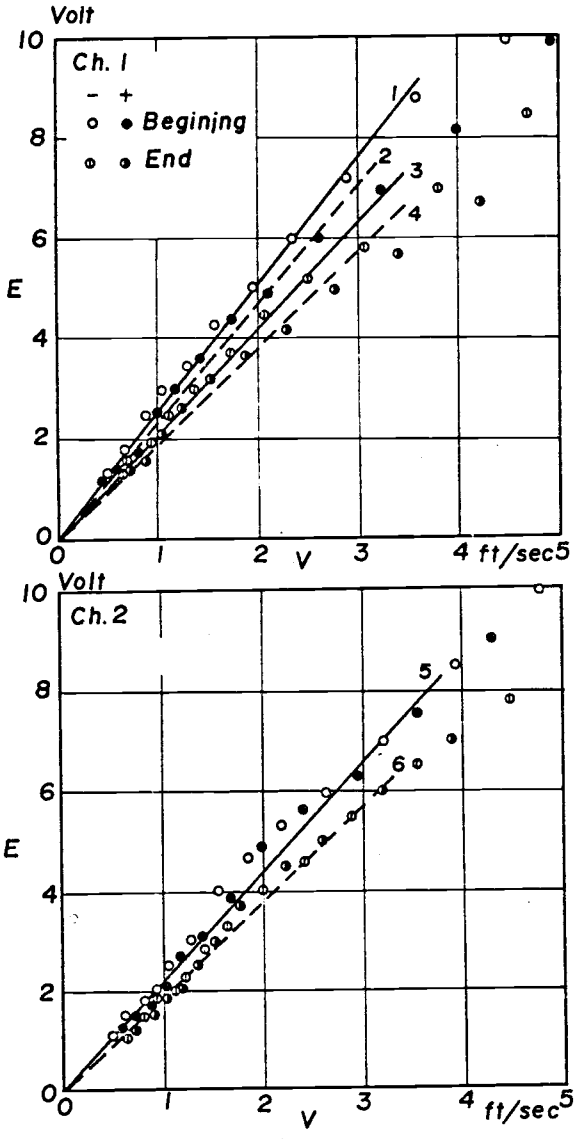

Fig. A.11 Calibration for periodic wave tests (Series I)

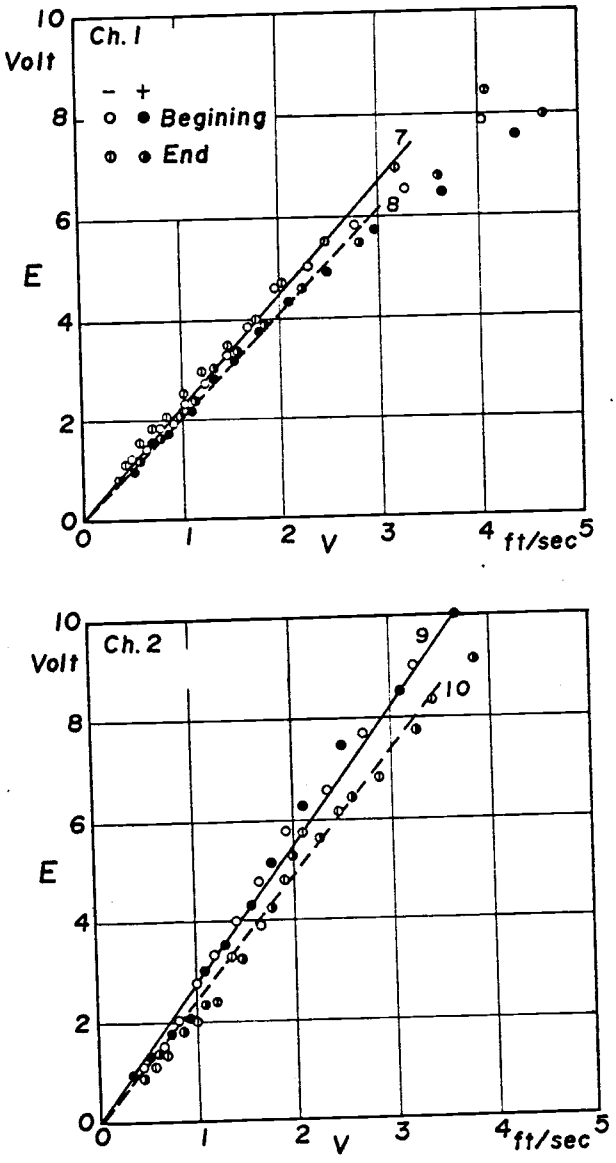

Fig. A.12 Calibration for periodic wave tests (Series II)

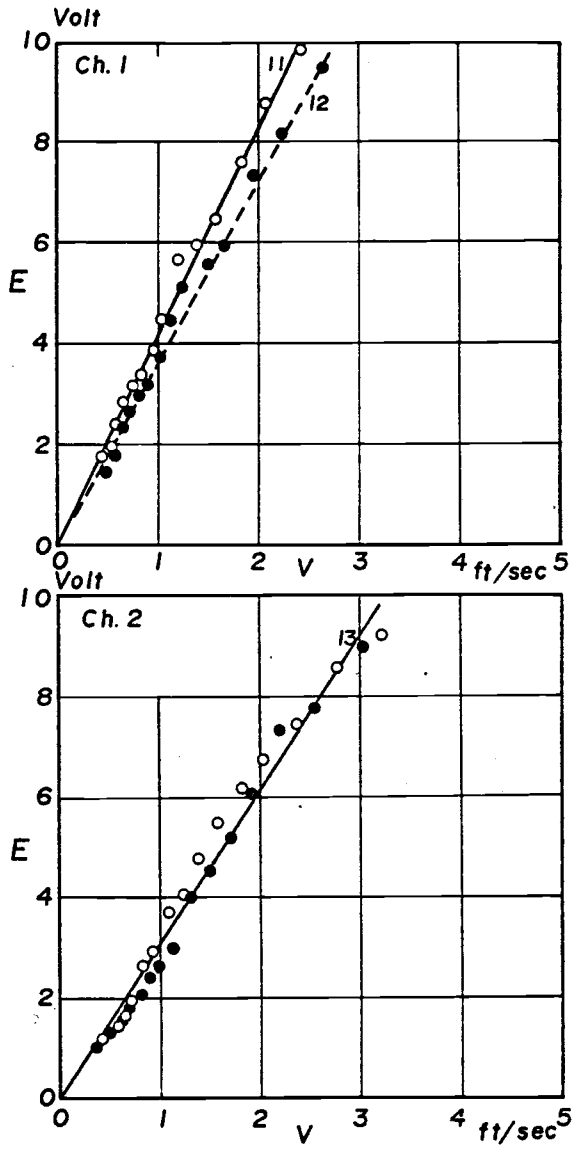

Fig. A. 13 Calibration for random wave tests (z= -2 ft)

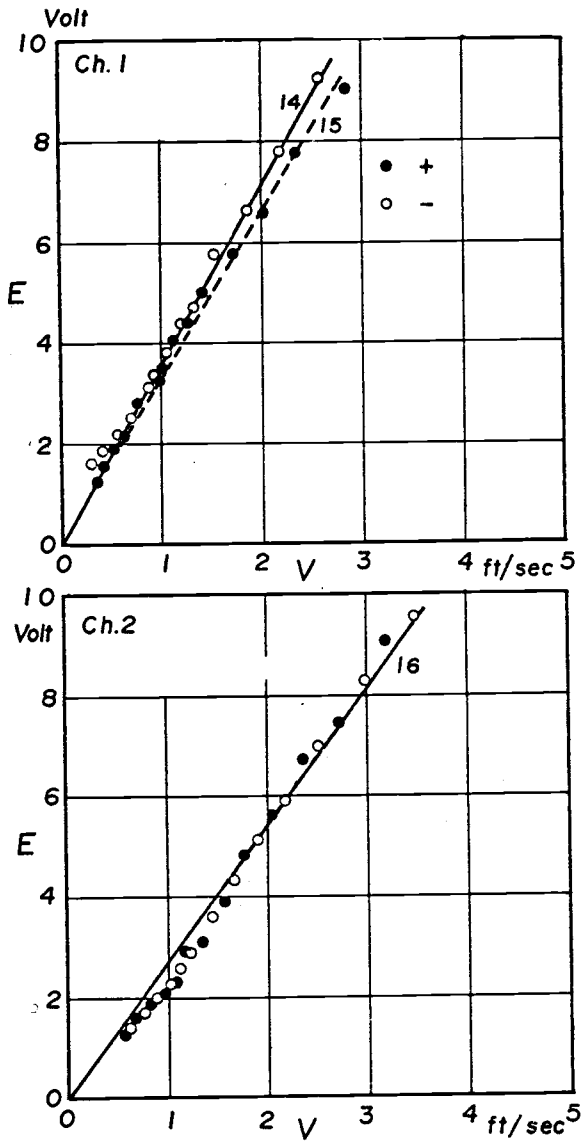

Fig. A.14 Calibration for random wave tests (z= -4 ft)

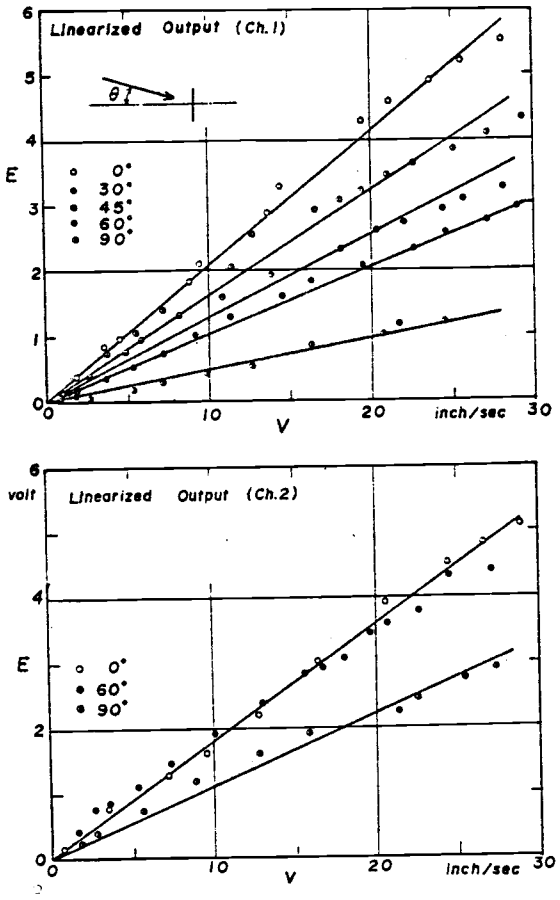

Fig. A.15 Angular sensitivity of hot film sensors